1   *Supplementary Information of*

2   **Global Nitrous Oxide Budget 1980-2020**

3   **Hanqin Tian et al.**

4   *Correspondence to:* Hanqin Tian (hanqin.tian@bc.edu)

5 Extended methodology

6

7 SI-1 NMIP-2: global Nitrogen/N₂O Model Inter-comparison Project phase 2

8

9 The NMIP2 is a follow-up model intercomparison project of NMIP (*Tian et al.*, 2018), which provides
10 estimates of N_2O emissions from natural and agricultural soils and covers the time period 1850-2020. Eight
11 process-based Terrestrial Biosphere Models (TBMs) participate in NMIP-2. In general, N_2O emissions
12 from soil are regulated at two levels, which are the rates of nitrification and denitrification in the soil and
13 soil physical factors regulating the ratio of N_2O to other nitrous gases (*Davidson et al.*, 2000). For N input
14 to land ecosystems, all eight models considered N fertilizer use, atmospheric N deposition and biological
15 fixation, but five models considered manure as N input. For vegetation processes, all models included
16 dynamic algorithms in simulating N allocation to different living tissues and vegetation N turnover, and
17 simulated plant N uptake using the "Demand and Supply-driven" approach. For soil N processes, all eight
18 models simulated N leaching according to water runoff rate; however, models are different in representing
19 nitrification and denitrification processes and the impacts of soil chemical and physical factors. The
20 differences in simulating nitrification and denitrification processes are one of the major uncertainties in
21 estimating N_2O emissions. Model characteristics in simulating major N cycling processes associated with
22 N_2O emissions in each participating model are briefly described in Table SI-1.

23

24 Table SI-1. Model characteristics in simulating major N cycling processes

	CLASS IC	DLEM	ELM	ISAM	LPX-Bern	O-CN	ORCHIDEE	VISIT
Open C cycle [a]	Yes	Yes	Yes	Yes	Yes	Yes	Yes	Yes
C-N coupling	Yes	Yes	Yes	Yes	Yes	Yes	Yes	Yes
N pools [b]	(3, 1, 3)	(6,6,8)	(6,4,5)	(6,4,4)	(4,3,8)	(9,6,9)	(9,6,9)	(4,1,4)
Demand and supply–driven plant N uptake	Yes	Yes	Yes	Yes	Yes	Yes	Yes	Yes
N allocation [c]	Dynamic	Dynamic	Dynamic	Dynamic	Dynamic	Dynamic	Dynamic	Dynamic
Nitrification	$f(T, SWC, C_{NH4})$	$f(T, SWC, C_{NH4})$	$f(T, SWC, pH, rh, C_{NH4})$	$f(T, SWC, C_{NH4})$	$f(T, SWC, C_{NH4})$	$f(T, SWC, pH, C_{NH4})$	$f(T, SWC, pH, C_{NH4})$	$f(T, SWC, pH, C_{NH4})$
Denitrification	$f(T, SWC, C_{NO3})$	$f(T, SWC, clay, rh, C_{NO3})$	$f(T, SWC, pH, rh, C_{NO3})$	$f(T, SWC, C_{NO3})$	$f(T, SWC, R_{mb}, C_{NO3})$	$f(T, SWC, pH, R_{mb}, C_{NO3})$	$f(T, SWC, pH, denitrifier, C_{NO3})$	$f(SWC, rh, C_{NO3})$
Mineralization, immobilization	$f(C:N)$	$f(C:N)$	$f(C:N)$	$f(C:N)$	$f(C:N)$	$f(C:N)$	$f(C:N)$	$f(C:N)$
N leaching	$f(runoff, C_{NO3}, C_{NH4})$	$f(runoff, C_{NO3}, C_{NH4})$	$f(runoff, C_{NO3})$	$f(runoff, C_{NO3}, C_{NH4})$	$f(runoff, C_{NO3})$	$f(runoff, C_{NO3}, C_{NH4})$	$f(runoff, C_{NO3}, C_{NH4})$	$f(runoff, C_{NO3})$
NH₃ volatilization	$f(C_{NH3})$	$f(T, SWC,$	No	$f(C_{NH3})$	$f(T, SWC,$	$f(C_{NH3})$	$f(SWC, pH, C_{NH4})$	$f(T, SWC,$

		pH, C_{NH4})			pH, C_{NH4})			pH, C_{NH4})
Plant N turnover [d]	Dynamic	Dynamic	Dynamic	Dynamic	Dynamic	Dynamic	Dynamic	Dynamic
N resorption	Fixed	f(C:N)	Fixed	f(C:N)	Fixed	Fixed	Fixed	Fixed
N fixation	f(N_limit)	f(T, SWC, C_NH4, C_NO3)	f(T, C:N)	f(ET)	Implied by mass balance	f(N_limit)	Fixed	f(ET)
N fertilizer use	Yes	Yes	Yes	Yes	Yes	Yes	Yes	Yes
Manure N use	No	Yes	No	Yes	No	Yes	Yes	Yes
N deposition	Yes	Yes	Yes	Yes	Yes	Yes	Yes	Yes

25 [a] "Open" denotes that excess N can be leached from the system.
26 [b] Numbers of N pools (vegetation pools, litter pools, soil pools).
27 [c] Dynamic denotes time-varied N allocation ratio to different N pools.
28 T: soil temperature, SWC: soil water content, clay: soil clay fraction, ET: evapotranspiration, denitrifier:
29 soil denitrifier biomass, rh: soil heterogeneous respiration, Nlimit: N limitation of vegetation growth,
30 C_{NO3}: soil NO_3^- content, C_{NH4}: soil NH_4^+ content.
31
32 All NMIP2 models are driven by consistent input datasets (i.e., climate, atmospheric CO_2 concentration,
33 land cover change, irrigation, atmospheric N deposition, mineral N fertilization, and manure N application
34 and deposition) and implemented consistent simulation experiments (SH0 – SH12; Table A4). Nitrogen
35 inputs data used in NMIP2 simulations are from History of anthropogenic Nitrogen inputs (HaNi) dataset
36 (*Tian et al.*, 2022), which takes advantage of different data sources in a spatiotemporally consistent way to
37 generate a set of high-resolution (5 arcminutes) gridded N input products from 1850 to 2020. HaNi data set
38 shows that the total anthropogenic N inputs to global terrestrial ecosystems increased from 29.05 Tg N yr^{-1}
39 in the 1860s to 267.23 Tg N yr^{-1} in the 2010s, with the dominant N source changing from atmospheric N
40 deposition (before the 1900s) to manure N (the 1910s-2000s), and to synthetic fertilizer in the 2010s (Fig.
41 B3). The climate data used to run historical simulations is the half degree CRU-JRA2.2 6-hourly forcing
42 over 1901- 2020 (https://catalogue.ceda.ac.uk/uuid/4bdf41fc10af4caaa489b14745c665a6). Annual CO_2
43 concentration during 1850-2020 were derived from ice core CO_2 data and NOAA annual
44 observations(https://www.esrl.noaa.gov). Historical distribution of cropland, pasture, rangeland and
45 irrigation during 1850-2020 were from Land-Use Harmonization 2 (LUH2) dataset (*Hurtt et al.*, 2020). The
46 original dataset of LUH2 is at a resolution of 0.25° x 0.25° longitude/latitude. We aggregated all geo-
47 referenced input data into a consistent spatial resolution of 0.5° x 0.5° longitude/latitude to run NMIP2
48 models.
49
50 NMIP2 models perform a subset of 13 simulations (SH0-SH12) to quantify N_2O emissions from both
51 agricultural and natural soils during the study period, and to disentangle the effects of multiple
52 environmental factors on soil N_2O emissions. The SH1 results were taken as the "best estimates" of soil
53 N_2O emissions because they include the effects of all driving factors that models can take into account. In
54 the SH0 simulation, driving forces were kept constant at the level in 1850 over the entire simulation period
55 (1850-2020). According to previous N_2O budget studies, atmospheric N_2O growth rate and Monte-Carlo
56 method, we suggest the following criteria for the N_2O budget inclusion (Table A6), and the criteria for
57 carbon components are consistent with TRENDY. By comparing results from factorial simulation
58 experiments (SH0 - SH12), we attribute changes in soil N_2O emissions to seven natural and anthropogenic
59 factors, namely, climate (CLIM, including precipitation, humidity, temperature and photosynthetic active
60 radiation changes), atmospheric CO_2 concentration (CO_2), land cover change (LCC), irrigation (IRRI),

61 atmospheric N deposition (NDEP), mineral N fertilizer use (NFER), and manure N use in cropland
62 (MANN). In order to understand soil N_2O emissions dynamics caused by crop cultivation, we further
63 separate the global and regional N_2O emissions into those derived from cropland soils and those from soils
64 of other land ecosystems. In this study, we attribute the impact of a single factor on cropland N_2O emissions.
65 Five models (DLEM, ISAM, O-CN, ORCHIDEE, and VISIT) considered the effects of manure N
66 application in cropland, therefore, we use these five models' results to calculate the manure N effect (SH1-
67 SH2). Meanwhile, we used results from all the eight models (i.e., CLASSIC, DLEM, ELM, ISAM, LPX-
68 Bern, O-CN, ORCHIDEE, and VISIT) to calculate the effects of synthetic N fertilizer use (SH1-SH3) and
69 atmospheric N deposition (SH1-SH4). The effect of N deposition in natural ecosystems (SH1-SH4) and the
70 effects of CO_2 (SH1-SH7) and climate (SH1-SH8) on global terrestrial ecosystems are calculated from the
71 eight NMIP2 models mentioned above.
72
73
74 **Table SI-2. Criteria for the N_2O budget inclusion**

Carbon criteria	N_2O criteria
(1) Steady state after spin-up, diagnosed from SH0 run: steady-state defined as an offset < 0.10 PgC yr^{-1}, drift < 0.05 PgC yr^{-1} per century (i.e. first is the average over 1850-2020, second is the slope x 100).	(1) Steady state after spin-up, diagnosed from SH0 run: drift < 0.2 Tg N_2O-N yr^{-1} per century (i.e. the slope x 100).
(2) Net annual land flux is a carbon sink over the 1990s and 2000s as constrained by global atmospheric and oceanic observations (Keeling & Manning, 2014), diagnosed from SH3 run.	(2) Inside the present-day (2007-2016) land emission range: 7-13 Tg N_2O-N yr^{-1}, diagnosed from SH1 run. The upper limit was calculated using the maximum total N_2O emissions minus the minimum estimates of other sources, and the lower limit was calculated using the minimum total N_2O emissions minus the maximum estimates of other sources. The range of total emissions was estimated by a one-box model using atmospheric N_2O growth rate, and the range of the sum of other sources was calculated by a Monte-Carlo method using estimates from Tian et al. (2020).
	(3) Inside the pre-industrial land emission range: 3 to 9 Tg N_2O-N yr^{-1}, diagnosed from SH1 run. This range is derived from the pre-industrial atmospheric burden/N_2O lifetime minus ocean and river/ coastal/estuary emissions (Michael J. Prather et al., 2015).

75
76
77 **Brief description of algorithms associated with N_2O flux in each NMIP2 model:**

78 **1: CLASSIC**

79 The representation of nitrogen cycling in CLASSIC is described in *Asaadi and Arora* (2021) and *Kou*
80 *Giesbrecht and Arora* (2022). N_2O production due to both nitrification and denitrification are represented.
81 N_2O loss during nitrification (I_{N_2O}; g N m^{-2} d^{-1}) is represented with the following equation:
82 $$I_{N_2O} = \eta_{N_2O} f_I(T_{0.5}) f_I(\psi) N_{NH_4} \qquad (1)$$
83 η_{N_2O} is a coefficient (d^{-1}), $f_I(T_{0.5})$ is a dimensionless scalar that depends on soil temperature averaged over
84 the top 0.5m soil depth ($T_{0.5}$), $f_I(\psi)$ is a dimensionless scalar that depends on soil matric potential (ψ), and
85 N_{NH_4} is the soil ammonium pool (g N m^{-2}).

86 N$_2$O loss during denitrification (E_{N_2O}; g N m^{-2} d^{-1}) is represented with the following equation:

87 $$E_{N_2O} = \mu_{N_2O} f_E(T_{0.5}) f_E(\theta) N_{NO_3} \tag{2}$$

88 μ_{N_2O} is a coefficient (d^{-1}), $f_E(T_{0.5})$ is a dimensionless scalar that depends on soil temperature averaged over
89 the top 0.5m soil depth ($T_{0.5}$), $f_E(\theta)$ is a dimensionless scalar that depends on soil moisture (θ), and N_{NO_3}
90 is the soil nitrate pool (g N m^{-2}).

91
92 **2: DLEM**

93 The nitrogen cycle scheme in DLEM2.0 (*Xu et al.*, 2017; *Yang et al.*, 2015; Tian et al. 2020) are similar as
94 DLEM1.0 (*Lu and Tian*, 2013; *Tian et al.*, 2012b; *Tian et al.*, 2010; *Tian et al.*, 2011; *Xu et al.*, 2011),
95 However, the N$_2$O emission schemes in DLEM2.0 (*Xu et al.*, 2017) have been modified based on *Chatskikh*
96 *et al.* (2005) and *Heinen* (2006).

97
98 $$R_{nit} = k_{nit\_max} f(T1) f(WFPS) C_{NH4} \tag{3}$$

99
100 $$R_{den} = k_{den\_max} f(T2) f(WFPS) C_{NO3} \tag{4}$$

101
102 where R_{nit} is the daily nitrification rate (g N/m^2/d); R_{den} is the daily denitrification rate (g N/m^2/d);
103 $f(T1)$ and $f(T2)$ are the impact function of daily soil temperature on nitrification and denitrification,
104 respectively; $f(WFPS)$ is the impact function of water-filled pore space (WFPS) on nitrification,
105 denitrification and N$_2$O diffusion; k_{nit_max} is the maximum fraction of NH$_4^+$-N that is converted to NO$_3^-$-
106 N or gases (0-1); k_{den_max} is the maximum fraction of NO$_3^-$-N that is converted to gases (0-1); C_{NH4} and
107 C_{NO3} are the soil NH$_4^+$-N and NO$_3^-$-N content (g N/m^2). N$_2$O from denitrification and nitrification processes
108 are calculated as,

109
110 $$R_{N2O} = (R_{nit} + R_{den}) f(T3) (1 - f(WFPS)) \tag{5}$$

111
112 where R_{N2O} is the daily N$_2$O emission rate (g N/m^2/d); $f(T3)$ is the impact function of daily soil
113 temperature on N$_2$O diffusion rate from soil pores. The calculation methods for these functions and
114 parameters were described in detail in *Xu et al.* (2017) and *Yang et al.* (2015).

115
116 **3: ELM**

117 The nitrogen dynamics in ELM is simulated based on the theory of equilibrium chemistry approximation
118 (*Zhu et al.*, 2016). Plants, soil microbes, and abiotic factors such as mineral surfaces coexist in the same
119 soil environment and vie for a diverse array of nutrients, including NH4+, NO3-. Due to the limited
120 availability of these nutrients, intense competitive interactions are expected. The competition of those
121 limited resources is represented by consumer–substrate networks, therefore, the uptake of nutrient substrate
122 by each consumer is dependent on the relative competitiveness of one consumer over the others. Nutrient
123 consumers' competitiveness is parametrized with kinetic parameters (Zhu et al., 2016). As a result, neither
124 plan nor soil microbes get the first priority to access nutrient substrates. Instead, when the potential nutrient
125 demands (from all nutrient consumers) exceed the supply at a given time step, the allocation of limited
126 nutrients among the consumers affects their performance (e.g., plant growth, soil organic matter
127 accumulation, nitrification, denitrification rates). ELM adopts a multiple-consumer-multiple-substrate
128 competition network (Zhu et al., 2016; Zhu et al., 2019) to simulate (1) nitrogen uptake facilitated by
129 nitrogen carrier enzymes, (2) binding of a nutrient substrate to a particular enzyme precludes it from
130 attaching to other enzymes, and (3) rates and affinities of consumers for different substrates. After the
131 nutrient competition has been resolved, scaling terms ($f(ECA_{nit})$ and $f(ECA_{den})$) will be applied to the
132 potential nitrification and denitrification processes:

133
134 $$R_{nit} = k_{nit\_max} f(\theta) f(T) (1 - f(O)) f(ECA_{nit}) C_{NH4} \tag{6}$$

135

136 $$R_{den} = min\ (f(deomp), f(C_{NO3}))f(ECA_{den}) \tag{7}$$

137

138 where k_{nit_max} is the maximum nitrification rate, $f(\theta)$, $f(T)$, $f(O)$ are soil moisture, temperature, and
139 oxygen scalars, respectively. $f(deomp)$ and $f(C_{NO3})$ are carbon limited and NO3- limited denitrification
140 rates (*Del Grosso et al.*, 2000).

141

142 **4: ISAM**

143 ISAM model contains detailed calculations of the terrestrial ecosystem's organic and mineral N cycle (*Yang*
144 *et al.*, 2009). The major N processes in ISAM include biological fixation, leaching, mineralization and
145 immobilization, plant uptake, nitrification, and denitrification. The soil biogeochemistry module of ISAM
146 shares the same ten soil layers (to 3.5 m depth) as the soil biogeophysics and calculates the vertical transport
147 of SOC and N (*Shu et al.*, 2020; *Yang et al.*, 2009). N$_2$O emission in ISAM N$_2$O is produced as a byproduct
148 of nitrification and denitrification (*Xu et al.*, 2021). N$_2$O module explicitly accounts for the vertical transport
149 of C, N, and O$_2$ within every soil layer for both saturated and unsaturated soil conditions by accounting for
150 the process of oxygen diffusing into the soil from the atmosphere and the soil oxygen supply. The model
151 also explicitly accounts for the effects of anoxic and oxic environments on nitrification (N$_{ni}$, Eq. 6) and
152 denitrification (N$_{de}$, Eq. 7). Both environments are calculated based on the fraction of anoxic soil depending
153 on soil O$_2$ concentration, which is non-linearly correlated with the chemical pathways forming N$_2$O.

154

155 $$N_{ni} = NH_4^+ \times (1 - e^{-F_{te\_m} \times F_{sm\_m} \times r_{ni}}) \times F_{pH\_m\_ni} \times R_d \tag{8}$$

156

157 $$N_{de} = NO_3^- \times r_{de} \times Rh \times F_{pH\_m\_de} \times R_d \tag{9}$$

158

159 where NH_4^+ and NO_3^- are ammonium and nitrate pool sizes; F_{te_m} is temperature modifier; F_{sm_m} is soil
160 moisture modifier; r_{ni} and r_{de} are base nitrification and denitrification rates; $F_{pH\_m\_ni}$ and $F_{pH\_m\_de}$ are pH
161 modifiers for nitrification and denitrification; R_d is relative soil anoxic fraction; Rh ($= 1\text{-}R_d$) is heterotrophic
162 respiration.

163

164 Under anoxic soil conditions, N$_2$O is produced through denitrification, while under oxic soil conditions,
165 more N$_2$O is produced from nitrification. The model accounts for soil NH$_4^+$ volatilization at the soil surface
166 when NH$_4^+$ in NH$_4^+$-containing fertilizers (e.g., urea) is converted to ammonia gas, depending upon pH
167 (*Huang and Gerber*, 2015). The soil NH$_4^+$ volatilization in the model is also affected by the anoxic
168 condition, which increases under a higher temperature and relatively lesser soil anoxic condition. The model
169 accounts for the impacts of pH on nitrification, denitrification, and volatilization rates (*Li et al.*, 2000; *Xu-*
170 *Ri and Prentice*, 2008). We prescribe the soil pH from the Global Soil Dataset for Earth System Modeling
171 dataset (GSDE) (*Shangguan et al.*, 2014).

172

173 **5: LPX-Bern**

174 The implementation of nitrogen dynamics in LPX-Bern is based on the work of *Xu-Ri and Prentice* (2008).
175 Nitrogen uptake by plants is governed by their demand and the availability of nitrogen in two soil pools
176 representing ammonium and nitrate. Nitrogen from deposition and fertilization are added to these inorganic
177 soil pools. Losses include ammonium volatilization, nitrate leaching as well as N$_2$O and NO production
178 during nitrification and N$_2$O, NO and N$_2$ production during denitrification. Aerobic nitrification of
179 ammonium is dependent on soil temperature (T_{soil}) and indirectly on soil water content due to the
180 partitioning of wet and dry soil:

181

182 $$R_{nit} = max_{nit} f_1(T_{soil}) C_{NH4,dry} \tag{10}$$

183

184 where $max_{nit} = 0.92\ day^{-1}$ is the daily maximum nitrification rate at 20°C.
185 Anaerobic denitrification of nitrate in wet soil depends on labile carbon availability and soil temperature:
186
187 $$R_{den} = R_{mb}/(R_{mb} + K_{mb})f_2(T_{soil})C_{NO3,wet}/(C_{NO3,wet} + K_n) \tag{11}$$
188
189 The parameters K_{mb} and K_n are taken from *Xu-Ri and Prentice* (2008) and R_{mb} is the microbiotical soil
190 respiration. The amount of nitrogen lost as N₂O due to nitrification and denitrification is modelled as a
191 function of soil temperature, water content and the respective process rate.
192
193 **6: O-CN**

194 The treatment of inorganic soil nitrogen dynamics in O-CN follows largely *Xu-Ri and Prentice* (2008). O-
195 CN (*Zaehle and Friend*, 2010) considers N losses to NH₃ volatilisation, NOx, N₂O and N₂ production and
196 emission, as well as NH₄ and NO₃ leaching. Inorganic nitrogen dynamics in the soil are tightly coupled to
197 plant uptake and net mineralization. The anaerobic volume fraction of the soil is estimated by an empirical
198 function of the fractional soil moisture content (*Zaehle et al.*, 2011). The fraction of ammonium in the
199 aerobic part of the soil is subject to nitrification, according to:
200
201 $$R_{nit} = vmax_{nit}f(T1)f(pH1)C_{NH4} \tag{12}$$
202
203 where *f(pH1)* is the soil pH response functions for nitrification (*Li et al.*, 1992; *Xu-Ri and Prentice*, 2008),
204 and *vmax_{nit}* is the maximum daily nitrification rate under 20°C and favourable pH conditions (*Xu-Ri and*
205 *Prentice*, 2008).
206
207 Gross denitrification of the fraction of nitrate under anoxic conditions is modelled as:
208
209 $$R_{den} = R_{mb}/(R_{mb} + K_{mb})f(T2)f(pH2)C_{NO3}/(C_{NO3} + K_n) \tag{13}$$
210
211 where *f(pH2)* is the soil pH response functions for denitrification (*Li et al.*, 1992; *Xu-Ri and Prentice*, 2008),
212 R_{mb} is the soil microbial respiration rate, and K_{mb} and K_n parameters taken from *Li et al.* (1992).
213
214 The N₂O production from nitrification and denitrification is then calculated as:
215
216 $$R_{N2O} = a_{nit}f(T1)R_{nit} + b_{den}f(T2)f(pH3)R_{den} \tag{14}$$
217
218 where *a_{nit}* and *b_{denit}* are fraction loss constants, *f(pH3)* is a pH-modifier changing the degree of denitrification
219 producing N₂O versus NOₓ or N₂ (*Zaehle et al.*, 2011). Emissions of volatile compounds are simulated
220 using the empirical emission of *Xu-Ri and Prentice* (2008).
221
222 **7: ORCHIDEE**

223 Modeling of the mineral N dynamics by the ORCHIDEE model originates from the formulations used in
224 the O-CN (*Zaehle and Friend*, 2010). It is composed of five pools for ammonium/ammoniac, nitrate, NOx,
225 nitrous oxide, and di-nitrogen forms. N₂O production in both nitrification and denitrification processes are
226 represented.
227
228 The potential daily rate of nitrification, R_{nit}, occurs only on the aerobic fraction of the soil and is a function
229 of temperature, pH, and ammonium concentration (C_{NH4}):
230
231 $$R_{nit} = (1 - f(WFPS))f(T1)f(pH1)k_{nit}C_{NH4} \tag{15}$$
232
233 where k_{nit} is the reference potential NO3⁻ production per mass unit of ammonium.

7

234
235 **8: VISIT**

236 The nitrogen cycle scheme of VISIT is composed of three organic soil nitrogen pools (microbe, litter, and
237 humus), two inorganic soil nitrogen pools (ammonium and nitrate), and vegetation pools. Fertilizer is
238 considered as an input to the ammonium and nitrate pools at a fixed ratio, and manure as an input into the
239 litter organic nitrogen pool. N_2O emissions through nitrification and denitrification are estimated using the
240 scheme developed by *Parton et al.* (1996). Nitrification-associated N_2O emission ($R_{nit,N2O}$) is evaluated as
241 follows,
242
243 $$R_{nit,N2O} = f(WFPS)f(pH1)f(T1)(K_{max} + F_{max}f(NH4)) \tag{16}$$
244
245 where K_{max} is the soil-specific turnover coefficient; F_{max} is the parameter of maximum nitrification gas flux;
246 and $f(NH_4)$ is the effect of soil ammonium on nitrification. Denitrification-associated N_2O emission
247 ($R_{den,N2O}$) is evaluated by the following equation:
248
249 $$R_{den,N2O} = R_{den}(1 + R_{N2/N2O}) \tag{17}$$
250
251 $$R_{den} = min\,(f(NO_3), f(CO_2)) \times f(WFPS) \tag{18}$$
252
253 where $R_{N2/N2O}$ is the fractionation coefficient, which is also a function of WFPS, soil nitrate, and
254 heterotrophic respiration, $f(NO_3)$ is the maximum denitrification rate in high soil respiration rate
255 condition, $f(CO_2)$ is the maximum denitrification rate in high NO_3^- levels, and $f(WFPS)$ is the effect of
256 WFPS on denitrification rate.
257
258 N_2O production by nitrification ($R_{N2O,nit}$, g N-N_2O/m^2/d) is expressed as a function of the potential daily rate
259 of nitrification (R_{nit}, g N-NO_3^-/m^2/d), temperature and the water content as shown in *Zhang et al.* (2002).
260
261 $$R_{N2O,nit} = f(WFPS)f(T1)R_{nit}p_{N2O,nit} \tag{19}$$
262
263 where $p_{N2O,nit}$ (g N-N_2O (g N-NO_3^-)$^{-1}$) is the reference N_2O production per mass unit of NO_3^- produced by
264 nitrification. The denitrification occurs on the anaerobic fraction of the soil which is computed as a function
265 of the water-filled porosity ($f(WFPS)$) and is controlled by temperature, pH, soil NO concentration and
266 denitrifier microbial activity (a_{microb}, g m^{-2}) (*Li et al.*, 2000).
267
268 $$R_{N2O,den} = f(WFPS)f(T2)f(pH)f(NO)p_{N2O,den}a_{microb} \tag{20}$$
269
270 where $f(NO)$ is a Michaelis-Menten shape function and $p_{N2O,den}$ is the reference N_2O production per mass
271 unit of denitrifier microbes.
272
273 **SI-2 The FAOSTAT inventory**

274 The FAOSTAT emissions data (*FAO*, 2022) are computed at Tier 1 following *IPCC* (2006), Vol.
275
276 4. The overall equation is as follows:
277 Direct emissions are estimated at the country level, using the formula:
278
279 $$Emission = A * EF \tag{21}$$
280
281 where emission represents kg N yr^{-1}; *A* represents the amount of N in the following items (annual synthetic
282 N applications/manure applied to soils/manure left on pasture/manure treated in manure management

283 systems/crop residue/biomass burned amount) in kg N yr^{-1}; EF = Tier 1, default IPCC emission factors,
284 expressed in kg N/kg N.
285
286 Indirect emissions are estimated at the country level, using the formula:
287
288 $$Emission = A_{v\&l} * EF \qquad\qquad (22)$$
289
290 where emission represents kg N yr^{-1}; $A_{v\&l}$ represents the fraction of manure/synthetic N fertilizers that
291 volatize as NH_3 and NO_x and are lost through runoff and leaching in kg N yr^{-1}; EF = Tier 1, default IPCC
292 emission factors, expressed in kg N/kg N.
293
294 Synthetic N fertilizers: N_2O from synthetic fertilizers is produced by microbial processes of nitrification
295 and denitrification taking place on the addition site (direct emissions), and after volatilization/redeposition
296 and leaching processes (indirect emissions).
297
298 Manure management: The term manure includes both urine and dung (i.e., both liquid and solid material)
299 produced by livestock. N_2O is produced directly by nitrification and denitrification processes in the manure,
300 and indirectly by nitrogen (N) volatilization and redeposition processes.
301 Manure applied to soils: N_2O is produced by microbial processes of nitrification and denitrification taking
302 place on the application site (direct emissions), and after volatilization/redeposition and leaching processes
303 (indirect emissions).
304
305 Manure left on pastures: N_2O is produced by microbial processes of nitrification and denitrification taking
306 place on the deposition site (direct emissions), and after volatilization/redeposition and leaching processes
307 (indirect emissions).
308
309 Crop Residue: N_2O emissions from crop residues consist of direct and indirect emissions from nitrogen (N)
310 in crop residues left on agricultural fields by farmers and from forages during pasture renewal (following
311 the definitions in the IPCC guidelines (*IPCC*, 2006)). Specifically, N_2O is produced by microbial processes
312 of nitrification and denitrification taking place on the deposition site (direct emissions), and leaching
313 processes (indirect emissions).
314
315 Cultivation of organic soils: The FAOSTAT domain "Cultivation of organic soils" contains estimates of
316 direct N_2O emissions associated with the drainage of organic soils – histosols – under cropland and grazed
317 grassland.
318
319 Burning-savanna: N_2O emissions from the burning of vegetation biomass in the land cover types: Savanna,
320 Woody Savanna, Open Shrublands, Closed Shrublands, and Grasslands. Burning-crop residues: N_2O
321 produced by the combustion of a percentage of crop residues burnt on-site. Burning-biomass: N_2O
322 emissions from the burning of vegetation biomass in the land cover types: Humid tropical forests, other
323 forests, and organic soils.
324
325 **SI-3 The EDGAR v7.0 inventory**

326 The new online version, EDGAR v7.0 (https://edgar.jrc.ec.europa.eu/dataset_ghg70) incorporates a full
327 differentiation of emission processes with technology-specific emission factors and additional end-of-pipe
328 abatement measures and as such updates and refines the emission estimates. The emissions are modelled
329 based on the latest scientific knowledge and available global statistics primarily from International Energy
330 Agency (*IEA*, 2021) for energy related sectors, FAO statistics (*FAO*, 2022) for agriculture, which were
331 complemented for the rest of sectors with United States Geological Survey (USGS), International Fertiliser
332 Association (IFA), Gas Flaring Reduction Partnership (GGFR)/U.S. National Oceanic and Atmospheric

333 Administration (NOAA) and World Steel Association (worldsteel) recent statistics; the methods are those
334 recommended by *IPCC* (2006). Official data submitted by the Annex I countries to the United Nations
335 Framework Convention on Climate Change (UNFCCC) and to the Kyoto Protocol are used to some extent,
336 particularly regarding control measures implemented since 1990 that are not described by international
337 statistics. A fast-Track approach was used to extend the N_2O emission time series for the latest years up to
338 2021 (*Crippa et al.*, 2021; *Crippa et al.*, 2022).

340 The N_2O emission factors for direct soil emissions of N_2O from the use of synthetic fertilizers, from manure
341 used as fertilizers, and from crop residues are taken from *IPCC* (2006), which updated the default IPCC
342 emission factor in the IPCC Good Practice Guidance (2000) with a 20% lower value. N_2O emissions from
343 the use of animal waste as fertilizer are estimated considering both the loss of N that occurs from manure
344 management systems before manure is applied to soils and the additional N introduced by bedding material
345 (*Janssens-Maenhout et al.*, 2019). N_2O emissions from fertilizer use and CO_2 from urea fertilization are
346 estimated based on IFA and FAO recent statistics.

348 N_2O emissions from manure management are based on the distribution of manure management systems
349 from Annex I countries reporting to the UNFCCC, *Zhou et al.* (2007) for China and *IPCC* (2006) for the
350 rest of the countries.

352 Different N_2O emission factors are applied to tropical and non-tropical regions. N and dry matter content
353 of agricultural residues are estimated from the cultivation area and yield for 24 crop types from *FAO* (2022)
354 and using emission factors of *IPCC* (2006).

356 Indirect N_2O emissions from leaching and runoff of nitrate are estimated from N input to agricultural soils.
357 Leaching and runoff are assumed to occur in all agricultural areas except non-irrigated dryland regions,
358 which are identified with maps of FAO Geonetwork (https://www.fao.org/land-water/databases-and-
359 software/geonetwork/en/). The fraction of N lost through leaching and runoff is based on the study of *Van*
360 *Drecht et al.* (2003). The updated emission factor for indirect N_2O emissions from N leaching and run-off
361 from the *IPCC* (2006) guidelines is selected, while noting that it is 70% lower than the mean value of the
362 1996 IPCC Guidelines and the IPCC Good Practice Guidance *IPCC* (1996; 2000).

364 Indirect N_2O emissions from atmospheric deposition of N of NO_x and NH_3 emissions from non-agricultural
365 sources, mainly fossil fuel combustion, are estimated using N in NO_x and NH_3 emissions from these sources
366 as activity data, based on EDGAR v7.0 database for these gases. The same emission factor from *IPCC*
367 (2006) is used for indirect N_2O from atmospheric deposition of N from NH_3 and NOx emissions, as for
368 agricultural emissions (*Janssens-Maenhout et al.*, 2019).

370 The uncertainties for EDGAR N_2O emissions estimated by *Solazzo et al.* (2021) are based primarily on the
371 uncertainties in emissions factors and activity data statistics from the *IPCC* (2006). Globally, these
372 emissions are accurate within an interval of ±113 for energy, -12% to +16% for industrial processes and
373 product use, -225 to +302 for agriculture, -159% to 203% for waste and ±112% for others; the most
374 uncertain emissions are those related to N_2O from waste and agriculture.

376 **SI-4 The UNFCCC inventory (need description of UNFCCC)**

377 The UNFCCC collects detailed data on GHG emissions from its parties. Following extensive guidance
378 developed by IPCC (*Buendia et al.*, 2019; *Eggleston et al.*, 2006), parties to the convention prepare national
379 GHG inventories, including emissions (and sinks) of N_2O. All anthropogenic activities are covered, in
380 agriculture both direct and indirect N_2O emissions are included. While IPCC basically provides emission
381 factor approaches, parties are encouraged to take account of national specificities, use national factors and
382 data, wherever available, or develop emission models, with adequate scientific proof provided.

383 Combustion-related emissions and emissions from industrial processes may take advantage of emission
384 monitoring or specific plant operation conditions, if provided. Emission processes that are not associated
385 with anthropogenic activities are also not covered in the inventories.
386
387 Obligations and quality of data provided differ strongly by country category. High scrutiny is put on GHG
388 inventories from countries listed in Annex-I of the convention (Annex-I countries include most European
389 countries, U.S. and Canada, Australia and New Zealand, and Japan). Annex-I countries are obliged to
390 provide annual national inventories in considerable detail and have to be very transparent also in terms of
391 methodology used and underlying information. Each year, time-series of emissions and underlying data
392 since 1990 (in a few cases, alternative base years are used) up to the pre-previous year are freshly provided
393 in April each year (e.g., in April 2023 data up to the year 2021 had to be provided), leading to a
394 homogeneous data series. Reports and emission data are provided (to UNFCCC, and to all users from the
395 UNFCCC web site at https://unfccc.int/reports) in standardized format such that they can be transferred to
396 databases. National results are routinely being checked and evaluated by expert teams in form of specific
397 internal and external audits to assure data quality and consistency.
398
399 National information is highly relevant also for non-Annex I countries to the UNFCCC and is being
400 collected and distributed by UNFCCC as well. Requirements are much less stringent, however, as parties
401 are expected to provide data only according to their own capabilities and the support they get from other
402 countries. The so-called Biannual Update Reports are to be prepared every other year only. While in
403 principle following the same IPCC guidance, commitments to format, timing, and quality assessment are
404 by far less stringent, and the own ambition level of the respective party (country) may determine much of
405 the outcome. In any case, self-reporting of a country always also means the party is willing to take the
406 responsibility of the emissions reported.
407
408 The "EDGAR/UNFCCC" dataset used in this paper utilizes the database for Annex-1 countries for
409 emissions from fossil-fuel consumption, industrial processes, waste and wastewater, and merges with the
410 respective set derived from EDGARv7.0 for all remaining countries.
411
412 **SI-5 The SRNM model:** Flux upscaling model

413 The SRNM model (Wang et al., 2020) was applied to simulate direct cropland-N_2O emissions. In SRNM,
414 N_2O emissions were simulated from N application rates using a quadratic relationship, with spatially
415 variable model parameters that depend on climate, soil properties, and management practices. The original
416 version of SRNM was calibrated using field observations only from China (Zhou et al., 2015). In this study,
417 we used the global N_2O observation dataset to train it to create maps of gridded annual emission factors of
418 N_2O and the associated emissions at 5-minute resolution from 1901 to 2014(Cui et al., 2021). The gridded
419 EF and associated direct cropland-N_2O emissions are simulated based on the following equation:
420
421

422 $$E_{ijt} = \alpha_{ij}N_{ijt}^2 + \beta_{ij}N_{ijt} + \varepsilon_{ijt}, \quad \forall i \tag{23}$$

423 where

424 $$\alpha_{ij} \sim N\left(\sum_k \left(x_k\lambda_{ijk}\right), \sigma_{ijk}^2\right), \quad \beta_{ij} \sim N\left(\sum_k \left(x_k\phi_{ijk}\right), \sigma_{ijk}'^2\right) \tag{24}$$

425 $$\lambda_{ijk} \sim N\left(\mu_{ijk}, \omega_{ijk}^2\right), \quad \phi_{ijk} \sim N\left(\mu_{ijk}', \omega_{ijk}'^2\right), \quad \varepsilon_{ijt} \sim N\left(0, \tau^2\right) \tag{25}$$

426 and i denotes the sub-function of N_2O emission (i=1, 2, …, I) that applies for a sub-domain division W_i of
427 six climate or soil factors, j represents the type of crop (j=1-2, 1 for upland crops and 2 for paddy rice), k is
428 the index of climate or soil factors (k=1-6, i.e., soil pH, clay content, SOC, BD, the sum of cumulative

429   precipitation and irrigation, mean daily air temperature). W_i denotes a set of the range of multiple x_k. E_{ijt}
430   denotes direct N_2O emission flux (kg N ha^{-1} yr^{-1}) estimated for crop type j in year t in the ith sub-domain,
431   N_{ijt} is N application rate (kg N ha^{-1} yr^{-1}), and a_{ij} and b_{ij} are defined as summation of the product of x_k and l_{ijk}
432   over k. The random terms l and f are assumed to be independent and normally distributed, representing the
433   sensitivity of a and b to x_k. e is the model error. m and $m\not c$ are the mean effect of x_k for a and b, respectively.
434   s, $s\not c$, w, $w\not c$, and t are standard deviations. Optimal sub-domain division, associated parameters mean
435   values and standard deviations were determined by using the Bayesian Recursive Regression Tree version
436   2 (BRRT v2), constrained by the extended global cropland-N_2O observation dataset. The detailed
437   methodological approach of the BRRT v2 is described by Zhou et al (2015).
438
439   **Global cropland N_2O observation dataset**

440   We aggregated cropland N_2O flux observation data from 180 globally distributed observation sites from
441   online databases, on-going observation networks, and peer-reviewed publications (Figure SI-1). Chamber-
442   based observations were only included in this dataset. These data repositories are as follows: the
443   NitroEurope, CarbonEurope, GHG-Europe (EU-FP7), GRACEnet, TRAGnet, NANORP, and 14 meta-
444   analysis datasets (*Decock*, 2014; *Harris et al.*, 2014; *Helgason et al.*, 2005; *Hénault et al.*, 2005; *Hickman*
445   *et al.*, 2014; *Kim et al.*, 2013a; *Kim et al.*, 2013b; *Lehuger et al.*, 2011; *Leppelt et al.*, 2014; *Rochette and*
446   *Janzen*, 2005; *Sacks et al.*, 2010; *Shcherbak et al.*, 2014; *Stehfest and Bouwman*, 2006; *Walter et al.*, 2015).
447   Four types of data were excluded from our analysis: (i) observations without a zero-N control for
448   background N_2O emission, (ii) observations from sites that used controlled-release fertilizers or nitrification
449   inhibitors, (iii) observations not covering the entire crop growing season, (iv) observations made in
450   laboratory or greenhouse. We then calculated cropland-N_2O emissions as the difference between observed
451   N_2O emission (E) and background N_2O emission (E$_0$). Values of EF were estimated for each nonzero N
452   application rate (N_a) as direct cropland-N_2O emission divided by N_a: $EF = (E - E_0)/N_a$. This yielded a
453   global dataset of direct cropland-N_2O emissions, N-rate-dependent N_2O EFs and fertilization records from
454   each site (i.e., 1,052 estimates for upland crops from 152 sites and 154 estimates for paddy rice from 28
455   sites), along with site-level information on climate, soils, crop type, and relevant experimental parameters.
456   Total numbers of sites and total measurements in the dataset were more than doubled those for previous
457   datasets of N_2O EF. The extended global N_2O observation network covered most of fertilized croplands,
458   representing a wide range of environmental conditions globally. For each site in our dataset, the variables
459   included four broad categories: N_2O emissions data, climate data (cumulative precipitation and mean daily
460   air temperature), soil attributes (soil pH, clay content, SOC, BD), and management-related or experimental
461   parameters (N application rate, crop type). More details on global cropland N_2O observation dataset can be
462   found in *Cui et al.* (2021).
463

464
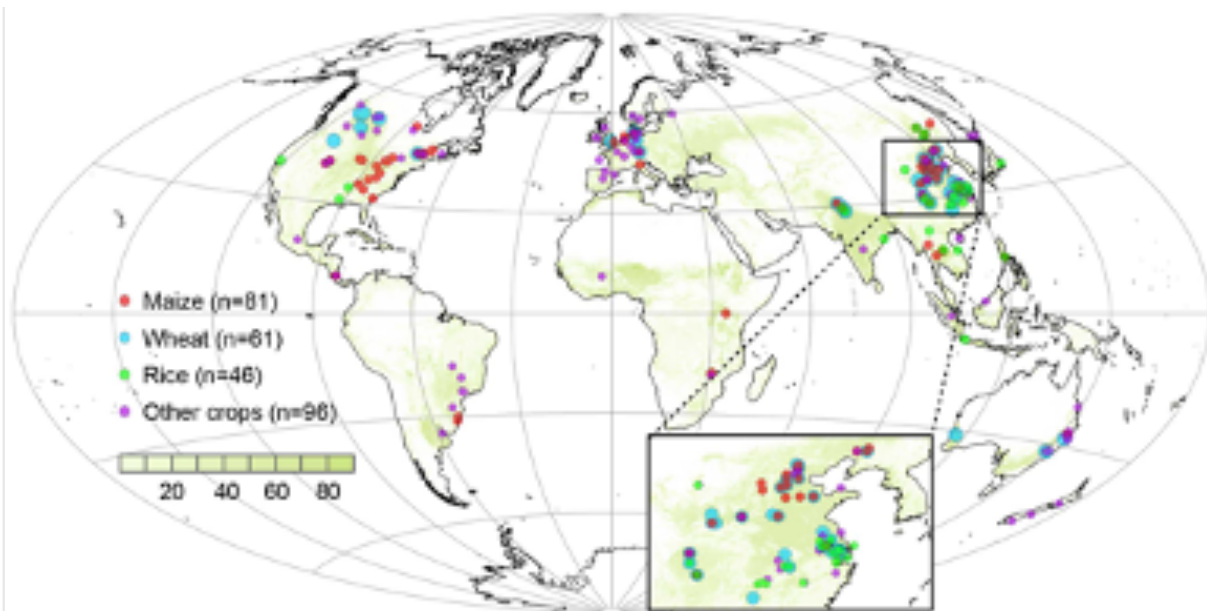
Figure SI-1 Global observation dataset of N$_2$O EF for direct soil emissions. Green area indicates the harvested areas of all crops derived from the Earthstat. Sites are indicated in different colors for maize, wheat, rice, and other crops.

Gridded input datasets:

The updated SRNM model was driven by many input datasets, including climate, soil properties, agricultural management practices (e.g., fertilization, tillage, irrigation), as well as the historical distribution of cropland. Cumulative precipitation and mean daily air temperature over the growing season were acquired from the CRU TS V4.06 climate dataset (0.5-degree resolution) (*Harris et al.*, 2014), where growing season in each grid cell was identified following *Sacks et al.* (2010)The patterns of SOC, clay content, BD, and soil pH were acquired from the HWSD v1.2 ((*Berdanier and Conant*, 2012), 1-km resolution). Both climate and soil properties were re-gridded at 5-arc-minute spatial resolution using a first-order conservative interpolation widely used in the CMIP5 model intercomparison (*Yang et al.*, 2017). The annual cropland area at 5-arc-minute spatial resolution from 1961 to 2020 was obtained from the History Database of the Global Environment (HYDE 3.2.1) (*Goldewijk et al.*, 2017).

For fertilization, crop-specific N fertilizer inputs (including synthetic N fertilizers, crop residues and manure), fertilizer types, and placement during 1961-2020 were obtained from Adalibieke et al., (2023). The frequency (i.e., one or multiple times) of N fertilization were the same as *Cui et al.* (2021) and we assumed that the frequency remained constant during the study period. For tillage, the fraction of tillage by crop during 1961-2020 was obtained from Adalibieke et al., (2023), which was constructed with the country and province (or state) level no-tillage area data during 1961-2020 and downscaled to grid with the method of *Porwollik et al.* (2019). For irrigation, the History Database of the Global Environment (HYDE version 3.2) (*Goldewijk et al.*, 2017) and the MIRCA2000 dataset (*Portmann et al.*, 2010) were used to compile the global crop-specific irrigation proportion data from year 1961 to 2020. Categories of cropland in HYDE provided new distinctions with irrigated and rain-fed crops (upland crops, other than rice), irrigated and rain-fed rice during 1960-2017. The national-level dataset of "Agricultural area actually irrigated" was obtained from (*FAO*, 2022), which was used to scale the baseline year 2015 maps of irrigated area from HYDE over the period 2016-2020. The area of irrigated upland crops from HYDE was first disaggregated into 21 crops based on the irrigated proportion from MIRCA2000 for per grid cell. We assumed an even share of irrigated area by each upland crop during the period 1961-2020, like MIRCA2000. Finally, the crop-specific irrigated area was masked by reporting harvested area, then the irrigated proportion of each

13

497 crop can be calculated as the crop-specific irrigated area divided by the physical area of each crop. For rice,
498 we further divided irrigated rice into continuously and intermittently flooded systems as provided by *Cui*
499 *et al.* (2021), and we assumed that the irrigation proportion was kept the same during the study period.
500
501 **SI-6 Global N flow in aquaculture**

502 We applied the IMAGE-GNM aquaculture nutrient budget model for shellfish and finfish (*Bouwman et al.*,
503 2013; *Bouwman et al.*, 2011) to calculate the nutrient flows in aquaculture production systems. These flows
504 comprise feed inputs, retention in the fish, and nutrient excretion. Individual species within crustaceans,
505 seaweed, fish and molluscs are aggregated to the International Standard Statistical Classification of Aquatic
506 Animals and Plants (ISSCAAP) groups (*FAO*, 2022), for which production characteristics are specified.
507 Feed and nutrient conversion rates are used for each ISSCAAP group to calculate the feed and nutrient
508 intake based on production data from FAO (*FAO*, 2020). Feed types include home-made aquafeeds and
509 commercial compound feeds with different feed conversion ratios that also vary in time due to efficiency
510 improvement; in addition, the model accounts for algae in ponds, that are often fertilized with commercial
511 fertilizers or animal manure, consumed by omnivore fish species like carp. A special case is the filter-
512 feeding bivalves that filter seston from the water column, and excrete pseudofeces, feces and dissolved
513 nutrients. Based on production data and tissue/shell nutrient contents, the model computes the nutrient
514 retention in the fish. Using apparent digestibility coefficients, the model calculates outflows in the form of
515 feces (i.e., particulate nutrients) and dissolved nutrients. Finally, nutrient deposition in pond systems and
516 recycling are calculated. For computing the N_2O emissions, we consider the amount of N released to the
517 environment, i.e., the difference between N intake and N in the harvested fish, which includes all the
518 nutrient excretion. Since in pond cultures part of that N is managed, we made the amount of N recycling
519 explicit, as well as ammonia emissions from ponds. This is to avoid double counting when computing N_2O
520 emissions from crop production.
521
522 **SI-7 Continental Shelves N_2O fluxes**

523 N_2O emissions from the global ocean do not include the contribution from continental shelves and are added
524 here using the extended mask of *Laruelle et al.* (2017) to delineate the coastal ocean. This mask excludes
525 estuaries and inland water bodies, while its outer limit is set 300 km away from the shoreline. Within this
526 coastal ocean domain, gridded N_2O emissions were calculated using one data-driven estimate and three
527 high-resolution model estimates from two distinct models, all interpolated on the same 0.25° x 0.25° grid.
528 Models and data are each covering different time-periods and only one climatology is provided, keeping
529 the original timespan of each product: 1988-2017 for the observation-based product that relied on a random-
530 forest (RF) algorithm to interpolate N_2O data (*Yang et al.*, 2020) from the MEMENTO database (MEM-
531 RF) (*Kock and Bange*, 2015), 1998-2018 for the estimate relying on the high-resolution configuration
532 (*Berthet et al.*, 2019) of the global ocean-biogeochemical component of CNRM-ESM2-1 (CNRM-0.25°),
533 1998-2013 and 2006-2013 for the estimates relying on the ECCO-Darwin model running at 1/3° (ECCO-
534 Darwin1) and 1/6° (ECCO-Darwin2), respectively. The resulting climatology can be considered as broadly
535 representative of the last 2-3 decades. Each product is further described as follows:
536
537 **MEM-RF**

538 The N_2O air-sea flux reconstruction by *Yang et al.* (2020) is based on a synthesis of over 158,000
539 observations of N_2O mixing ratio, partial pressure, and concentration in the surface ocean from the
540 MEMENTO database (https://memento.geomar.de) (*Kock and Bange*, 2015) and additional cruises
541 (Dataset S1) (*Yang et al.*, 2020). N_2O measurements are converted to surface N_2O mixing ratio anomalies
542 using observations from the NOAA atmospheric flask dataset (*Hall et al.*, 2007), and extrapolated to a 0.25-
543 degree resolution global monthly climatology using an ensemble of 100 random forest realizations. The
544 random forest algorithm predicts N_2O mixing ratio anomalies based on their relationship to oceanographic
545 predictors that include hydrographic variables, nutrients, oxygen, chlorophyll, net primary production, and

546 seafloor depth. Reconstructed mixing ratio climatologies are used to estimate air-sea fluxes by applying a
547 commonly used gas exchange parameterization (*Wanninkhof*, 2014). Two formulations of piston velocity
548 are adopted: one based on a quadratic dependence on wind speed (*Wanninkhof*, 2014), and one that
549 explicitly accounts for bubble-mediated fluxes (*Liang et al.*, 2013). Sea ice cover, surface temperature,
550 salinity and atmospheric pressure are taken from ERA5 reanalysis (*Hersbach et al.*, 2017). Calculations are
551 performed with two high-resolution wind products (ERA5 and CCMP) that are available at 0.25, 6-hourly
552 resolution for the period from 1988 to 2017, yielding four permutations of the piston velocity. The resulting
553 ensemble of 400 global N_2O air–sea flux estimates is averaged in time to obtain monthly mean
554 climatologies. A description of the dataset and methods is presented in *Yang et al.* (2020). The code used
555 to produce these datasets is archived on a public GitHub repository at https://github.com/yangsi7/mapping-
556 ocean-n2o (DOI: 10.5281/zenodo.3757194).

557
558 **CNRM-0.25°**

559 N_2O fluxes have been inferred from the global ocean-biogeochemical component of CNRM-ESM2-1
560 (*Séférian et al.*, 2019) run at 0.25° horizontal resolution with 75 vertical levels in the ocean. This high-
561 resolution configuration is described in *Berthet et al.* (2019) and is based on the NEMOv3.6 oceanic model
562 (*Madec*, 2008), the multi-category sea ice model GELATOv6 (*Salas y Mélia*, 2002) and the PISCESv2-gas
563 model for marine biogeochemistry (*Aumont et al.*, 2015), which includes an updated version of (*Martinez-
564 Rey et al.*, 2015) for the marine N_2O module. The simulation was first spun-up during 300 years under
565 preindustrial conditions and then has been forced by the OMIP2-compliant JRA55-do-1-5 atmospheric
566 reanalysis (*Tsujino et al.*, 2020; *Tsujino et al.*, 2018) considering the historical evolution of CO_2 and N_2O
567 in the atmosphere since the year 1850. Boundary conditions for nitrogen deposition and riverine inputs are
568 prescribed from monthly climatologies. The suboxic production of N_2O uses the oxygen-dependent
569 formulation of *Jin and Gruber* (2003) and is enhanced at low oxygen concentrations. This formulation
570 encompasses N_2O production during remineralization, nitrification and grazing, as well as a sink term
571 corresponding to N_2O consumption under anoxic conditions by denitrification. The oceanic N_2O partial
572 pressure is computed based on the surface N_2O concentration and the N_2O solubility in the ocean. Sea-to-
573 air N_2O fluxes are then computed using the standard gas exchange parameterization of *Wanninkhof* (1992;
574 2014).

575
576 **ECCO-Darwin & ECCO2-Darwin**

577 To generate global air-sea fluxes of nitrous oxide (N_2O) from the global ocean we have used the ECCO-
578 Darwin Model (*Carroll et al.*, 2020). The ECCO-Darwin model is based on MITgcm and it has a nominal
579 horizontal resolution of 1/3 of a degree with 50 vertical levels where in the top 100 meters the model is
580 vertically resolved with 10-meter grid boxes. The ECCO-Darwin model is forced with an atmospheric
581 forcing corresponding to the 1992-present optimized with adjoint technique in order to realistically
582 represent the observed physical climate phenomena such as El Nino, the Pacific Decadal Oscillation, the
583 North Pacific "Warm Blob", etc. A more detailed description of the model forcing and the Darwin
584 biogeochemical model configuration used in this study can be found in *Carroll et al.* (2020).

585
586 The Darwin biogeochemical/ecological model (*Carroll et al.*, 2020; *Manizza et al.*, 2019) used for this
587 study carries 33 biogeochemical tracers to explicitly represent the cycle of carbon, oxygen, phosphorus,
588 silica, and iron in the global ocean. For this particular version of the model, we implemented a
589 parameterization of the oceanic cycle of N_2O using the scheme of *Nevison et al.* (2003)based on the oceanic
590 oxygen cycle previously represented in ECCO2-Darwin model (*Ganesan et al.*, 2020). The air-sea gas flux
591 of N_2O was parameterized according to *Wanninkhof* (1992). In addition, a thermal- only N_2O tracer (a tracer
592 in which biogeochemical sources and sinks are suppressed but with the same solubility as N_2O) was also
593 added to the model to isolate the process of ocean ventilation affecting the N_2O concentration in the ocean
594 at seasonal time scales as done in *Manizza et al.* (2012). The ECCO-Darwin numerical simulation was run

595   for the 1992-2014 period, but we discarded the inclusion of the output relative to the 1992-1996 period in
596   our analysis due to the model adjustment in this initial part of our numerical simulation.
597
598   **SI-8 Open Ocean N_2O fluxes**

599   N_2O is produced in the open ocean by microbial activity during organic matter cycling in the subsurface
600   ocean, and its production pathways are influenced by the local environmental oxygen level. In the oxic
601   ocean N_2O is produced as a byproduct during the oxidation of ammonia to nitrate, mediated by ammonia
602   oxidizing bacteria and archaea. N_2O is also produced and consumed in sub- oxic and anoxic waters through
603   the action of marine denitrifiers during the multi-step reduction of nitrate to gaseous N. The oceanic N_2O
604   distribution therefore displays significant heterogeneity with background levels of 10-20 nmol/l in the well-
605   oxygenated ocean basins, high concentrations (> 40 nmol/l) in hypoxic waters, and N_2O depletion in the
606   core of ocean oxygen minimum zones (OMZs).

607
608   For this synthesis open ocean N_2O emissions to the atmosphere were compiled from four global ocean
609   biogeochemistry models/Earth System models that simulate the production, consumption and circulation
610   of oceanic N_2O (Table 6). N_2O flux exchange between ocean and atmosphere is derived using gas-exchange
611   parameterizations applied to modeled surface ocean N_2O. Versions of the four submitting models also
612   participated in the previous N_2O budget synthesis (*Tian et al.*, 2020a). Model details and updates to the
613   previous N_2O budget synthesis are summarized below.
614   The models differ in aspects of physical configuration (e.g., spatial resolution), meteorological forcing
615   applied at the ocean surface, and in their parameterizations of ocean biogeochemistry; specific details on
616   individual models are provided in the publications listed in Table 1. Towards this N_2O budget synthesis,
617   modelling groups reported grid-resolved ($1° \times 1°$ horizontal resolution) monthly estimates of ocean-
618   atmosphere N_2O fluxes for the period 1980-2020 (or for as many years as possible in that period).

619
620   **U. Bern: Bern-3D**

621   N_2O fluxes are derived from the Bern-3D Earth System Model of Intermediate Complexity which includes
622   a prognostic marine biogeochemistry model (based on (*Parekh et al.*, 2008) and (*Tschumi et al.*, 2011)).
623   Configuration of the model for simulation of N_2O is outlined in *Battaglia and Joos* (2018). Model
624   simulations were run at a native resolution of horizontal resolution of 41 by 40 grid cells and 32
625   logarithmically scaled vertical layers. Modifications of the biogeochemistry model relevant for the N_2O
626   cycle include the assignment of organic matter remineralization to aerobic and anaerobic pathways
627   dependent on mean grid-cell dissolved oxygen level. N_2O is produced by nitrification as a product of
628   remineralization rate and a specified N_2O yield which has a functional form dependent on oxygen level (see
629   details in (*Battaglia and Joos*, 2018)). N_2O consumption by denitrification processes is represented by a
630   first-order kinetics formulation which also includes a dependence on local oxygen level to account for the
631   relative importance of denitrification-related N_2O production and consumption processes in each gridcell.
632   Measurements of dissolved N_2O (surface and interior) from the MEMENTO database (*Kock and Bange*,
633   2015) together with an ensemble of model runs are used to constrain the model parameters governing N_2O
634   production and consumption mechanisms. From a pre-industrial equilibrium state the model is forced by
635   historical CO2 emissions, non-CO2 radiative forcing, and land-use changes. N_2O in the atmosphere is
636   prescribed based on historical data.

637
638   **CNRM: CNRM-ESM2-1**

639   N_2O fluxes are provided by the CNRM-ESM2-1 Earth System model. The ocean model component is based
640   on NEMO Version 3.6 (*Madec et al.*, 2017) and coupled to the GELATO sea ice model (*Salas y Mélia*,
641   2002) Version 6 and the marine biogeochemical model PISCESv2-gas (*Aumont et al.*, 2015). The spatial
642   model resolution follows the eORCA1L75 grid, with a nominal horizontal resolution of $1°$ and with higher
643   resolution in the tropics (increasing to $\sim(1/3)°$). The model has 75 vertical levels with higher resolution

644 towards the ocean surface. The simulations were forced at the surface by the atmospheric state of JRA55-
645 do v1.5.0 (*Tsujino et al.*, 2018). Atmospheric N2O concentration is given as annual means as specified by
646 CMIP6 protocols and is linearly interpolated in time. Parameterization of the marine N2O cycle follows that
647 of *Martinez-Rey et al.* (2015) with some modifications. N2O production is driven by an oxygen-dependent
648 yield of N2O, which encompasses production from denitrification and nitrification processes. This
649 formulation also assumes a constant background yield representing N2O production by nitrification and a
650 consumption of N2O in suboxic conditions. Originally implemented by *Martinez-Rey et al.* (2015), the
651 marine N2O parameterization has benefited from a recoding and an improved calibration presented in
652 *Berthet et al.* (2023). Further details of the model biogeochemistry and configuration are provided by
653 *Séférian et al.* (2019) and *Berthet et al.* (2019).
654
655 **UVic2.9**

656 N2O model fluxes are derived from the UVic2.9, Earth System Model of Intermediate Complexity with
657 prescribed monthly climatological winds (*Kalnay et al.*, 1996) and ice sheets (*Peltier*, 2004), configuration
658 outlined in *Landolfi et al.* (2017). Oceanic subsurface N2O production is parameterized following (*Zamora
659 and Oschlies*, 2014), as a function of O_2 consumption with a linear O_2 dependency, inherently including
660 both nitrification and denitrification. In O_2-deficient waters (<4 mmol m^{-3}), denitrification becomes a sink
661 of N2O consumed at a constant rate. The gradient driving the air-sea N2O gas exchange, is computed online
662 based on departure of the surface ocean concentration from the saturation value using the solubility
663 coefficients of *Weiss and Price* (1980) and time-varying prescribed atmospheric N2O concentrations
664 (historical and RCP8.5). The model was spun-up for 6000 years with preindustrial boundary conditions
665 (solar and volcanic and aerosol forcing, fixed atmospheric CO_2 of 280 ppm and N2O of 276 ppb, and
666 preindustrial atmospheric N deposition).
667

668 **UEA: NEMO-PlankTOM10.2**

669 N2O model fluxes are derived from the NEMO-PlankTOM10.2 ocean model. The physical circulation
670 component is NEMO v3.1 (*Madec*, 2008), with horizontal resolution of 2° longitude, and a variable
671 latitudinal resolution (average ~1°) with higher resolution in the tropics and polar regions. The model has
672 30 vertical layers, with variable resolution ranging from 10m in the upper 100m to 500m at depths of 5000
673 m. The biogeochemical component relies on the marine ecosystem model PlankTOM10, which includes
674 representation of 10 plankton functional types (*Le Quéré et al.*, 2016). It has been extended by *Buitenhuis
675 et al.* (2018) to include nitrogen cycle processes, and prognostic and diagnostic models of N2O production.
676 N2O is produced from nitrification and denitrification pathways, with oxygen dependent yields employed
677 to account for varying production and consumption processes in hypoxic waters. Nitrogen cycle parameters
678 are optimized using ocean databases of dissolved N2O (MEMENTO, *Kock and Bange* (2015)) nitrification
679 rates (*Yool et al.*, 2007), and surface ammonium concentrations (*Johnson et al.*, 2015; *Paulot et al.*, 2015).
680 Further details on model configuration are provided in (*Buitenhuis et al.*, 2018).
681

682 **SI-9 Net N2O emission from land cover change**

683 This section mainly involves the calculation of post-deforestation N2O emissions, deforestation induced
684 N2O reduction and N2O emissions from forest regrowth (afforestation or reforestation). The methods
685 include both bookkeeping and process-based modeling.
686

687 **a. Deforestation area, crop/pasture expansion and secondary forests**
688 The LUH2 v2h (land use harmonization, http://luh.umd.edu) land use data was used to derive the
689 deforestation area and its partition between crops and pastures during 1860−2020. LUH2 categorizes forest
690 lands into forested primary land and potentially forested secondary land, while croplands are divided into
691 C3 annual crops, C3 perennial crops, C4 annual crops, C4 perennial crops, and C3 N-fixing crops.
692

693   In the empirical computation of deforestation induced N_2O emissions, all sub-classes within each land use
694   type were treated the same. Thus, only the annual transition area from forests to croplands or managed
695   pasture was needed. In the process-based estimates, the DLEM model was improved to further account for
696   the classifications of primary forests, secondary forests (further partitioned into established and newly
697   converted by an age threshold of 15 years), croplands/pastures /rangelands (further partitioned into
698   established and newly converted by an age threshold of seven nine years). Each land use type can be divided
699   into several different plant functional types (PFTs). Specifically, within a grid cell, cropland can only be
700   dominated by only one crop type. The pastures and rangelands can be either C3 type or C4 type. To generate
701   the historical spatial distribution of PFTs, a potential vegetation map and the accompanied composition
702   ratio map of each natural PFT acquired from the Synergetic Land Cover Product (SYNMAP) were jointly
703   used with LUH2 v2h.
704
705 **b. Methods**
706   The bookkeeping method was mainly applied to the tropical areas, where forests generally have high N_2O
707   emissions. Specifically, the average tropical forest N_2O emission rate of 1.974 kg N_2O-N ha-1 yr-1 was
708   adopted as the baseline. Two logarithmic response curves of soil N_2O emissions (normalized to the baseline)
709   after deforestation were developed: $y = -0.31\ln(x) + 1.53$ and $y = -0.454\ln(x) + 2.21$. This form of the
710   response functions can effectively reproduce the short-lived increase in soil N_2O emissions after initial
711   forest clearing and the gradually declining emission rates of converted crops/pastures (*Melillo et al.*, 2001;
712   *Verchot et al.*, 1999). Using these two curves and the baseline, we kept track of the N_2O reduction of tropical
713   forests and the post-deforestation crop/pasture N_2O emissions at an annual timescale.
714
715   There are not many studies on N_2O emissions from secondary tropical forests that regrowth after crop or
716   pasture abandonment. *Sullivan et al.* (2019) lumped together all forms of N "gas loss" including NO and
717   N_2O for secondary forests across the tropics and the results showed gas loss gradually increases with age
718   since the regrowth of secondary forest. *Keller and Reiners* (1994) also reported a gradual recovery of soil
719   nitrate and soil emissions of N_2O and nitric oxide (NO) during 20 years of secondary forest succession,
720   which however did not return to the level of the primary forests. In this study, using field observations from
721   *Davidson et al.* (2007) and *Keller and Reiners* (1994), we regressed normalized N_2O emissions (relative to
722   a reference mature forest) of secondary tropical forests with their ages as $y=0.0084x + 0.2401$ ($R^2 = 0.44$;
723   unit of x is year). The derived y values were multiplied by tropical forest N_2O emissions estimated by
724   NMIP2 models that do not distinguish secondary forests from primary forests.
725
726   The DLEM model was run with varying climate and CO_2 with other factors held constant to estimate forest
727   baseline emissions and unfertilized crop/pasture emissions from 1860-2020. The climate data were acquired
728   from CRUJRA, which is a fusion of the CRU and JRA reanalysis products at a spatial resolution of 0.5° ×
729   0.5° and a daily time-step. The atmospheric CO_2 data were obtained from NOAA GLOBLVIEW-CO2
730   dataset (https://www.esrl.noaa.gov), which are derived from atmospheric and ice core measurements. In
731   the tropical area, both estimates from the DLEM model and the bookkeeping method were adopted, whereas
732   in extra-tropical area, we only adopted the DLEM outputs.
733
734 **SI-10 Inland water, estuaries, and coastal vegetation**
735
736 **a. Dynamic Land Ecosystem Model-Terrestrial/Aquatic Continuum (DLEM-TAC)**
737   To quantify N_2O emissions from global inland waters (rivers, lakes, and reservoirs), we use a process-based
738   coupled terrestrial-aquatic model, which builds up on the Dynamic Land Ecosystem Model (DLEM).
739   DLEM-TAC is a fully distributed, process-based land surface model which couples the major land
740   processes (terrestrial hydrology, plant phenology and physiology, soil biogeochemistry) and aquatic
741   dynamics (lateral transport and in-stream biogeochemistry) (*Pan et al.*, 2021; *Tian et al.*, 2015; *Tian et al.*,
742   2020b; *Yao et al.*, 2020). The land component of DLEM-TAC explicitly simulates the carbon, nitrogen,

743 and water fluxes between plants, soil, and atmosphere, and the surface and drainage runoff and nitrogen
744 load from the land module are used as   input for   the aquatic module. The simulated nitrogen load
745 includes dissolved inorganic nitrogen (DIN), dissolved organic nitrogen (DON), particulate organic
746 nitrogen (PON), and runoffs, sewers as the initial condition of the aquatic module.
747
748 DLEM-TAC aquatic module calculated lateral water transport and the associated aquatic biogeochemical
749 processes by adopting a scale-adaptive scheme. The water transport scheme, which coupled hillslope flow,
750 subnetwork flow, and main channel flow, simulated the water transport processes within grid cells. In the
751 aquatic module, lakes and reservoirs were linked with small streams and large rivers, forming a river-lake-
752 reservoir corridor (*Wollheim et al.*, 2008)). Particularly, lakes that are linked to small streams are typically
753 small in size and are defined as small lakes, while those linked to large rivers are usually had large size and
754 are defined as large lakes; similarly, reservoirs that are linked to main channels are considered as large
755 reservoirs, while those that are linked to small streams are considered as small reservoirs. The incoming
756 flow of a linked river-lake-reservoir corridor drains to lakes first, and the outflow rate of lakes and reservoirs
757 is determined based on the predefined residence time obtained from the global lake dataset (*Lehner et al.*,
758 2011; *Messager et al.*, 2016; *Yao et al.*, 2022). The aquatic N module was developed based on the scale
759 adaptive water transport scheme, including lateral transport, decomposition of organic matter, particle
760 organic matter deposition, nitrification, and denitrification. The detailed description could be found in the
761 previous studies (*Pan et al.*, 2021; *Tian et al.*, 2020b; *Yao et al.*, 2020).
762
763 Following our previous work referring to the development of water transport and biogeochemistry, we
764 developed an inland water N_2O module within the aquatic biogeochemical component of the DLEM
765 framework (*Yao et al.*, 2020). The net fluxes of dissolved N_2O (including physical and biogeochemical
766 processes) in the main channel (high-order streams) and subnetwork (small rivers) are estimated as:
767

$$(\Delta M\_N2O) / \Delta t = Fa + Ywater + D - R - E \tag{26}$$

768 where M_N2O is the total mass of dissolved N_2O in the main channel or subnetworks (g N), Δt is the time
769 step, Fa is advective N_2O fluxes (g N d^{-1}), Ywater is the N_2O production within the water column (g N d^{-1}),
770 D is the dissolved N_2O from rainfall to rivers (i.e. deposition) (g N d^{-1}) with an initial concentration equal
771 to the atmospheric equilibrium N_2O concentration, R is the flux from N_2O reduction (g N d^{-1}) to nitrogen
772 gas, and E is the riverine N_2O efflux (g N d^{-1}) through the air-water interface.
773
774 Input data. The driving data of DLEM-TAC include the climate variables, atmospheric CO2 concentration,
775 land use change, nitrogen (N) deposition, N fertilizer, and manure application with a spatial resolution of
776 0.5°× 0.5°. The daily climate variables (precipitation, mean temperature, maximum temperature, minimum
777 temperature, and shortwave radiation) were obtained from the CRUNCEP dataset
778 (https://vesg.ipsl.upmc.fr) for 1901-2019. Climate data of each year during 1850-1900 was randomly
779 sampled from 1901-1920. Annual atmospheric CO2 concentration from 1900-2019 was obtained from the
780 NOAA GLOBALVIEW-CO2 dataset (https://www.esrl.noaa.gov). The annual land use change data was
781 derived from a potential natural vegetation map (synergetic land cover product) and a prescribed cropland
782 area dataset from the history database of the global environment v.3.2 (HYDE 3.2, ftp://ftp.pbl.nl/hyde).
783 The data of N fertilizer, manure N application, and N deposition data was obtained from (*Tian et al.*, 2022).
784
785 In the aquatic module, the required channel dataset included channel slope, channel width, and channel
786 length generated from the Hydroshed dataset (*Lehner et al.*, 2008) and DDM30 dataset (*Döll and Lehner*,
787 2002). The flow direction and distance data were obtained from the Dominant River Tracing (DRT) dataset.
788 For modeling water dynamics in lakes and reservoirs, we generated 0.5 grid level surface water area,
789 upstream area, volume, depth, and average residence time for lakes based on the Hydrolakes dataset

790 (*Messager et al.*, 2016), while the GRanD database provided the same information for reservoirs (*Lehner*
791 *et al.*, 2011).
792
793 Simulation protocol. DLEM-TAC simulations include three steps: equilibrium run, spin-up run and two
794 transit runs, one with dam operation close, and another one with dam operation open. First, the equilibrium
795 run is required to obtain the initial and steady condition of carbon, nitrogen, and water pool at the pre-
796 industrial level in each grid cell (*Thornton and Rosenbloom*, 2005). In this step, we held all the driving
797 forces such as climate data, atmospheric CO_2 concentration, land use data, and nitrogen additions consistent
798 with the first year's data we used in the simulation. Second, we conducted a 30-year spin-up run by
799 randomly selecting climate data within the 1850s (*Tian et al.*, 2012a). This step can alleviate the disturbance
800 of driving data changes in the transit run. Then we conduct the natural flow simulation with the dam model
801 temporarily closed, and all the driving forces change over time. After the natural flow simulation, we set
802 up a management flow simulation with the dam module open, specifically the dam module needs natural
803 flow in the previous run as model input.
804
805 b. **Mechanistic Stochastic Modeling of N_2O emissions from large rivers, lakes, reservoirs, and**
806 **estuaries:**
807
808 To calculate the cascading loads of TN and TP delivered to each water body along the river–reservoir–
809 estuary continuum, we spatially routed all reservoirs from the GRanD database (*Lehner et al.*, 2011), with
810 river networks from Hydrosheds 15s (*Lehner et al.*, 2008) and, at latitudes above 50°N, Hydro1K
811 (http://edc.usgs.gov/products/elevation/gtopo30/hydro/), which were in turn connected to estuaries as
812 represented in the "Worldwide Typology of Nearshore Coastal Systems" of *Dürr et al.* (2011). In addition,
813 the global database HydroLAKES (*Messager et al.*, 2016) was used to topologically connect 1.4 million
814 lakes with a minimum surface area of 0.1 km^2 within the river network. Note that besides natural lakes,
815 HydroLAKES includes updated information on 6,796 reservoirs from the GRanD database, which was used
816 in the study of *Maavara et al.* (2019). In order to estimate the TN and TP loads to each water body, we then
817 relied on a spatially explicit representation of TN and TP mobilization from the watershed into the river
818 network (see (*Maavara et al.*, 2019) for details (*Bouwman et al.*, 2009; *Van Drecht et al.*, 2009).
819
820 For the estimation of N_2O emission, we applied two distinct model configurations, respectively named DS1
821 and DS2 in *Maavara et al.* (2019). DS1 estimates N_2O emissions from denitrification and nitrification based
822 on an EF of 0.9%, which is in the mean of published values (*Beaulieu et al.*, 2011), and the assumption that
823 N_2O production equals N_2O emissions (*Maavara et al.*, 2019). For DS2, the reduction of N_2O to N_2 during
824 denitrification if N_2O is not evading sufficiently rapidly from the water body is considered. The fluxes in
825 the model represent lumped sediment-water column rates and were resolved at the annual timescale. The
826 use of water residence time as an independent variable in both the mechanistic model and the upscaling
827 process introduces an important kinetic refinement to existing global N_2O emission estimates. Rather than
828 applying an average EF (directly scaling N_2O emissions to N inputs) to all water bodies, the use of water
829 residence time explicitly adjusts for the extent of N_2O production and emission that is kinetically possible
830 within the timeframe available in a given water body. Simulated N_2O emission rates were evaluated against
831 UNFCCC measurement-based upscaling methods applied to reservoirs (*Deemer et al.*, 2016) and rivers
832 (*Hu et al.*, 2016) as well as a UNFCCC observation-driven regional estimate of lake N_2O emissions based
833 on literature data (*Lauerwald et al.*, 2019).
834
835 **c. Meta analysis-based N_2O emissions from large rivers**
836 Data from 70 published studies between 1998 and 2016 that provided N_2O emission from streams and rivers
837 were compiled by *Hu et al.* (2016). The N_2O emission factors (EF = N_2O /DIN) and emission rates (ER =
838 EF * DIN load, kg N_2O-N yr^{-1}) were calculated for each studied river. Exploratory multiple regression
839 analyses were conducted to predict EF and ER using various combinations of factors (N concentrations,

840 loads, yields, DOC: DIN, discharge, and watershed area) and different functions. Among them, DIN yield
841 (kg N yr^{-1} km^{-2}) was identified as the best predictor of EF and ER. Using the optimal model and DIN loads
842 for 6400 global rivers calculated by the NEWS2-DIN-S model (*McCrackin et al.*, 2014), we estimated
843 global riverine N$_2$O emissions (*Hu et al.*, 2016).
844
845 **d. Stream and river N$_2$O emissions combining machine-learning and model-based upscaling**

846 *Marzadri et al.* (2021) developed a novel approach that combines a data-driven Random Forest Machine
847 Learning (RM-ML) model with a physically-based upscaling model to predict near global (neglecting
848 Arctic and Antarctic areas) riverine N$_2$O emissions flux (F*N$_2$O given by the ratio between the flux of N$_2$O,
849 FN$_2$O, and the in-stream flux of dissolved inorganic nitrogen species FDIN) from both surface (i.e. water
850 column) and subsurface (i.e. benthic zone and hyporheic zone) riverine environments. In particular, to
851 capture the local scale processes responsible for N$_2$O emissions and to provide estimations at different
852 spatial scales (from local reach up to the global scale) the model compute two different denitrification
853 Damköhler numbers (given by the ratio between a characteristics time of transport and a characteristics
854 time of denitrification (*Marzadri et al.*, 2021; *Marzadri et al.*, 2017)) starting from the hydro-morphological
855 and biogeochemical information provided by the RM-ML model. Model results at the local reach scale
856 shows that nearly 50% of the riverine N$_2$O emissions comes from small streams (i.e. widths lower than 10
857 m, although they represent only the 13% of the total riverine surface area worldwide) while at the large
858 scale predict a near-global annual riverine N$_2$O emissions around 72.8 GgN$_2$O$-$N/yr.
859

860 **e. Meta-analysis based N$_2$O emissions from estuaries and coastal vegetation**

861 N$_2$O emissions from estuaries and coastal vegetated ecosystems were obtained from a meta-analysis of
862 observed N$_2$O fluxes (*Rosentreter et al.*, 2023). In brief, the meta-data analysis relies on a categorization of
863 estuaries into 'tidal systems and deltas', 'lagoons', and 'fjords'. Water-air N$_2$O fluxes from 123 estuary
864 sites globally were then compiled from peer-reviewed publications until the end of 2020. Coastal vegetation
865 comprises 'mangrove', 'salt marsh', and 'seagrass' ecosystems and N$_2$O sediment-water-air fluxes were
866 compiled from 55 sites globally from peer-reviewed publications until the end of 2020. A non-parametric
867 bootstrapping method (1000 iterations of the median of samples) was used to resample N$_2$O fluxes per unit
868 area for each estuary and coastal vegetation type in each of the 18 regions using the 'boot' function in the
869 package 'boot' in R software. Results from the bootstrapping output (minimum, Q1, median, mean, Q3,
870 maximum) were then scaled to the surface area of each estuary and coastal vegetation type in each of the
871 18 RECCAP regions. If an ecosystem type had less than three sites in a region, we applied the global
872 statistics of this type in this region. Note that the meta-data analysis only provides flux assessments at the
873 scale of the 18 regions.
874

875 **SI-11 Atmospheric inversion models**

876 Emissions were estimated using four independent atmospheric inversion frameworks (see Table 1). The
877 frameworks all used a Bayesian inversion method. The approach used here finds the maximum posteriori
878 (MAP), or optimal, estimate of emissions, that is, those, which when coupled to a model of atmospheric
879 transport, provide the best agreement to observed N$_2$O mixing ratios while being guided by their prior
880 probability. In this particular case, where both the likelihood and prior probability are assumed to be
881 distributed normally, the optimal emissions are equivalent to those that minimize the cost function,
882

883
$$J(\mathbf{x}) = \frac{1}{2}(\mathbf{x} - \mathbf{x_b})^{T} \mathbf{B}^{-1}(\mathbf{x} - \mathbf{x_b}) + \frac{1}{2}(\mathbf{y} - H(\mathbf{x}))^{T} \mathbf{R}^{-1}(\mathbf{y} - H(\mathbf{x}))$$
(27)

884

885 where $\mathbf{x}$ and $\mathbf{x_b}$ are, respectively, vectors of the multivariate means of the posterior and prior emission
886 distributions, $\mathbf{B}$ is the prior error covariance matrix for emissions, $\mathbf{y}$ is a vector of observed N$_2$O mixing
887 ratios, $\mathbf{R}$ is the observation error covariance matrix, and $H(\mathbf{x})$ is the model of atmospheric transport (for

888 details on the inversion method see (*Tarantola*, 2005)). The optimal emissions, **x**, were found by solving
889 the first order derivative of equation (21):
890

891 $$J'(\mathbf{x}) = \mathbf{B}^{-1}\left(\mathbf{x} - \mathbf{x_b}\right) + \left(H'(\mathbf{x})\right)^{\mathrm{T}} \mathbf{R}^{-1}\left(\mathbf{y} - H(\mathbf{x})\right) = 0 \qquad (28)$$

892

893 where $(H'(\mathbf{x}))^{\mathrm{T}}$ is the sensitivity of the atmospheric observations to emissions, derived from an adjoint
894 model of transport. In frameworks INVICAT, PyVAR-CAMS and GEOS-Chem, equation (5b) was solved
895 using a variational approach (*Thompson et al.*, 2014; *Wells et al.*, 2015; *Wilson et al.*, 2014), which uses a
896 descent algorithm and computations involving the forward and adjoint models. In framework MIROC4-
897 ACTM (*Patra et al.*, 2018), equation (22) was solved directly by computing a transport operator, **H** from
898 integrations of the forward model, such that **Hx** is equivalent to $H(\mathbf{x})$, and taking the transpose of **H** (*Patra*
899 *et al.*, 2022).
900

901 Each of the inversion frameworks used a different model of atmospheric transport with different horizontal
902 and vertical resolutions (see Table 1). The transport models TOMCAT and LMDz5, used in INVICAT and
903 PyVAR-CAMS respectively, were driven by ECMWF ERA-5 and ERA-Interim wind fields respectively,
904 MIROC4-ACTM was driven by JRA-55 wind fields, and GEOS-Chem was driven by MERRA-2 wind
905 fields. While INVICAT, PyVAR-CAMS, and GEOS-Chem optimized the emissions at the spatial
906 resolution of the transport model, MIROC4-ACTM optimized the error in the emissions aggregated into 84
907 land and ocean regions. All frameworks optimized the emissions with monthly temporal resolution. The
908 transport models included an online calculation of the loss of N_2O in the stratosphere due to photolysis and
909 oxidation by $O(^1D)$ resulting in mean atmospheric lifetimes of between 118 and 129 years, broadly
910 consistent with recent independent estimates of the lifetime of 116±9 yr (*Prather et al.*, 2015)).
911

912 All inversions used N_2O measurements of discrete air samples from the National Oceanic and Atmospheric
913 Administration Carbon Cycle Cooperative Global Air Sampling Network (NOAA). In addition, discrete
914 measurements from the Commonwealth Scientific and Industrial Research Organisation network (CSIRO)
915 as well as in-situ measurements from the Advanced Global Atmospheric Gases Experiment network
916 (AGAGE), the NOAA CATS network, and from individual sites operated by University of Edinburgh (UE),
917 National Institute for Environmental Studies (NIES), the Finnish Meteorological Institute (FMI) and the
918 Japan Meteorological Agency (JMA) were included in INVICAT, PyVAR-CAMS and GEOS-Chem.
919 Measurements from networks other than NOAA were corrected to the NOAA calibration scale, NOAA-
920 2006A, using the results of the WMO Round Robin inter-comparison experiment
921 (https://www.esrl.noaa.gov/gmd/ccgg/wmorr/), where available. For AGAGE and CSIRO, which did not
922 participate in the WMO Round Robins, the data at sites where NOAA discrete samples are also collected
923 were used to calculate a linear regression with NOAA data, which was applied to adjust the data to the
924 NOAA-2006A scale. For the remaining CSIRO sites where there were no NOAA discrete samples, the
925 mean regression coefficient and offset from all other CSIRO sites were used. The inversions used the
926 discrete sample measurements without averaging, and hourly or daily means of the in-situ measurements,
927 depending on the particular inversion framework.
928

929 Each framework applied its own method for calculating the observation space uncertainty, the square of
930 which gives the diagonal elements of the observation error covariance matrix R. The observation space
931 uncertainty accounts for measurement and model representation errors and is equal to the quadratic sum of
932 these terms. Typical values for the observation space uncertainty were between 0.3 and 0.5 ppb for all
933 inversion frameworks.
934

935 Prior mean emissions were based on estimates from terrestrial biosphere and ocean biogeochemistry models
936 as well as from inventories. INVICAT, PyVAR-CAMS and GEOS-Chem used the same prior estimates for
937 emissions from natural and agricultural soils from the model OCN v1.1 (*Zaehle et al.*, 2011) and for biomass

938   burning emissions from GFEDv4.1s. For non-soil anthropogenic emissions (namely those from energy,
939   industry and waste sectors), INVICAT, PyVAR-CAMS, and GEOS-Chem used EDGAR v5. MIROC4-
940   ACTM used the VISIT model (*Inatomi et al.*, 2010; *Ito et al.*, 2018) for emissions from natural soils and
941   EDGAR 4.2 for all anthropogenic emissions, including agricultural waste burning, but did not explicitly
942   include a prior estimate for wildfire emissions.
943
944   For the prior mean estimate of ocean fluxes, INVICAT, PyVAR-CAMS and GEOS-Chem used the
945   prognostic version of the PlankTOM-v10.2 model (*Buitenhuis et al.*, 2018) with a global total source 2.5
946     $TgN \ yr^{-1}$. Prior uncertainties were estimated in all the inversion frameworks for each grid cell (INVICAT,
947   PyVAR-CAMS and GEOS-Chem) or for each region (MIROC4-ACTM) and the square of these
948   uncertainties formed the diagonal elements of the prior error covariance matrix **B**. INVICAT, PyVAR-
949   CAMS and GEOS-Chem estimated the uncertainty as proportional to the prior value in each grid cell, but
950   MIROC4-ACTM set the uncertainty uniformly for land regions at 1 Tg N yr^{-1} and for ocean regions at 0.5
951   Tg N yr^{-1}. INVICAT also included off-diagonal covariances in B corresponding to a spatial correlation
952   between flux uncertainties of 500 km and assumed a semi-exponential distribution of uncertainties so as to
953   restrict the possibility of negative fluxes.
954
955
956   **SI-12 Atmospheric N_2O Observation Networks**
957   The NOAA Network: For atmospheric N_2O observations from the NOAA network (Dutton et al. 2023), we
958   used global mean mixing ratios from the NOAA Global Monitoring Laboratory (GML) (combined dataset
959   based on measurements from five different measurement programs [HATS old flask instrument, HATS
960   current flask instrument (OTTO), the Carbon Cycle and Greenhouse Gases (CCGG) group Cooperative
961   Global Air Sampling Network (https://www.esrl.noaa.gov/gmd/ccgg/flask.php), HATS in situ (RITS
962   program), and HATS in situ (CATS program)]. CCGG provides uncertainties with each measurement (see
963   site files: ftp://aftp.cmdl.noaa.gov/data/greenhouse_gases/n2o/flask/surface/). The CCGG measurements
964   for N_2O analysis from more than 50 sites globally was changed to tunable infrared laser direct absorption
965   spectroscopy (TILDAS) in mid-2019 from gas chromatography. About 40 sites of them (mostly Marine
966   Boundary Layer sites) are used to calculate CCGG monthly mean global N_2O levels. Monthly mean
967   observations from different NOAA measurement programs are statistically combined to create a long-term
968   NOAA/ESRL GML dataset. Uncertainties (1 sigma) associated with monthly estimates of global mean
969   N_2O, are ~1 ppb from 1977−1987, 0.6 ppb from 1988−1994, 0.3−0.4 ppb from 1995−2000, and 0.1 ppb
970   from 2001-2017. NOAA data are generally more consistent after 1995, with standard deviations on the
971   monthly mean mixing ratios at individual sites of ~0.5 ppb from 1995−1998, and 0.1−0.4 ppb after 1998.
972   A detailed description of these measurement programs and the method to combine them are available via
973   https://www.esrl.noaa.gov/gmd/hats/combined/N2O.html.
974   THE AGAGE network: The Advanced Global Atmospheric Gases Experiment (AGAGE) global network
975   (and its predecessors ALE and GAGE) (Prinn et al., 2018) has made continuous high-frequency gas
976   chromatographic (GC) measurements with electronic capture detection (ECD) of N_2O at five globally
977   distributed sites since 1978. Improved GC/ECD methods have been deployed over time resulting in N_2O
978   measurement precision of about 0.35% in ALE, 0.13% in GAGE (Prinn et al., 1990) and 0.05% in AGAGE
979   (Prinn et al., 2008; 2018). We used the global mean of AGAGE N_2O measurements during 1980−2020
980   which are reported on the Scripps Institution of Oceanography SIO-16 scale. Further information on
981   AGAGE stations, instruments, calibration, uncertainties and access to data is available at the AGAGE Data
982   website: https://www.osti.gov/dataexplorer/biblio/dataset/1841748.
983
984   The CSIRO network: The CSIRO flask network (Francey et al., 2003) consists of nine sampling sites
985   distributed globally and has been in operation since 1992. Flask samples are collected approximately every
986   two weeks and shipped back to CSIRO GASLAB for analysis. Samples were analyzed by gas
987   chromatography with electron capture detection (GC-ECD). One Shimadzu gas chromatograph labelled
988   "Shimadzu-1" (S1) has been used over the entire length of the record and the measurement precision for

989   N_2O from this instrument is about 0.1%. N_2O data from the CSIRO global flask network are reported on
990   the NOAA-2006A N_2O scale and are archived at the World Data Centre for Greenhouse Gases (WDCGG:
991   https://gaw.kishou.go.jp/). Nine sites from the CSIRO network were used to calculate the annual global
992   N_2O mole fractions. Smooth curve fits to the N_2O data from each of these sites were calculated using the
993   technique outlined in Thoning et al. (1989), using a short-term cut-off of 80 days. The smooth curve fit data
994   were then placed on an evenly spaced latitude (5 degree) versus time (weekly) grid using the Kriging
995   interpolation technique. Finally, the gridded data were used to calculate the global annual values.
996
997   Table SI-3 Factors used to convert N_2O in various units (by convention Unit 1=Unit 2 × conversion)

Unit 1	Unit 2	Conversion
Tg N_2O (teragrams of N_2O)	Tg N (teragrams of nitrogen)	1.57
Tg N (teragrams of nitrogen)	g N (grams of nitrogen)	10^{-12}
Tg N (teragrams of nitrogen)	ppb (parts per billion)	4.79

998

999   Table SI-4 Atmospheric N_2O dry mole fraction measured by different observing networks during 2000-
1000   2022.

ppb	NOAA	AGAGE	CSIRO	Min	Max
2000	315.58	316.18	315.48	315.48	316.18
2001	316.33	316.95	316.12	316.12	316.95
2002	316.99	317.54	316.67	316.67	317.54
2003	317.64	318.26	317.31	317.31	318.26
2004	318.24	318.99	317.99	317.99	318.99
2005	318.98	319.71	318.83	318.83	319.71
2006	319.93	320.39	319.58	319.58	320.39
2007	320.59	321.16	320.34	320.34	321.16
2008	321.54	322.11	321.45	321.45	322.11
2009	322.24	322.91	322.22	322.22	322.91
2010	323.04	323.77	323.08	323.04	323.77
2011	324.21	324.68	324.09	324.09	324.68
2012	325.01	325.65	324.99	324.99	325.65
2013	325.92	326.61	325.89	325.89	326.61
2014	327.06	327.66	326.93	326.93	327.66
2015	328.13	328.52	327.99	327.99	328.52
2016	328.94	329.36	328.77	328.77	329.36
2017	329.75	330.37	329.68	329.68	330.37

2018	330.87	331.53	330.90	330.87	331.53
2019	331.85	332.35	331.66	331.66	332.35
2020	333.06	333.48	332.70	332.70	333.48
2021	334.33	334.81	334.03	334.03	334.81
2022	335.71	336.09	335.57	335.57	336.09

1001

1002

1003 Table SI-5: Uncertainty in future projections of atmospheric N_2O dry mole fraction.

ppb	SSP1-1.9		SSP1-2.6		SSP2-4.5		SSP3-7.0		SSP4-3.4		SSP4-6.0		SSP5-8.5	
Year	Min	Max	Min	Max	Min	Max	Min	Max	Min	Max	Min	Max	Min	Max
2020	330.4	331.1	330.4	331.1	331.0	331.6	331.4	332.0	331.2	331.5	331.2	331.4	331.2	331.9
2030	335.1	336.9	335.5	337.0	337.6	339.6	339.5	342.2	337.5	338.6	338.8	339.6	339.5	341.1
2040	336.2	341.1	336.8	342.0	343.2	347.3	347.9	353.4	340.5	345.7	346.3	349.2	349.2	350.7
2050	336.2	344.6	337.8	345.7	348.5	354.3	356.1	364.9	343.3	353.3	353.5	359.2	359.4	361.2

1004

1005 **References:**

1006

1007 Adalibieke, W., Cui X.Q., Cai H.W., You L.Z., and Zhou F.: Global crop-specific nitrogen fertilization
1008 dataset in 1961-2020, Scientific Data 10, 617, 2023, https://www.nature.com/articles/s41597-023-02526-z

1009 Asaadi, A., and Arora, V. K.: Implementation of nitrogen cycle in the CLASSIC land model,
1010 *Biogeosciences*, *18*(2), 669-706, 2021.

1011 Aumont, O., Éthé, C., Tagliabue, A., Bopp, L., and Gehlen, M.: PISCES-v2: an ocean biogeochemical
1012 model for carbon and ecosystem studies, *Geoscientific Model Development Discussions*, *8*(2), 1375-1509,
1013 2015.

1014 Battaglia, G., and Joos, F.: Marine N2O emissions from nitrification and denitrification constrained by
1015 modern observations and projected in multimillennial global warming simulations, *Global Biogeochemical*
1016 *Cycles*, *32*(1), 92-121, 2018.

1017 Beaulieu, J. J., Tank, J. L., Hamilton, S. K., Wollheim, W. M., Hall Jr, R. O., Mulholland, P. J., Peterson,
1018 B. J., Ashkenas, L. R., Cooper, L. W., and Dahm, C. N. : Nitrous oxide emission from denitrification in
1019 stream and river networks, *Proceedings of the National Academy of Sciences*, *108*(1), 214-219, 2011.

1020 Berdanier, A. B., and Conant, R. T.: Regionally differentiated estimates of cropland N2O emissions reduce
1021 uncertainty in global calculations, *Global Change Biology*, *18*(3), 928-935, 2012.

1022 Berthet, S., Jouanno, J., Séférian, R., Gehlen, M., and Llovel, W.: How does the phytoplankton–light
1023 feedback affect the marine N2O inventory?, *Earth System Dynamics*, *14*(2), 399-412, 2023.

1024 Berthet, S., Séférian, R., Bricaud, C., Chevallier, M., Voldoire, A., and Ethé, C.: Evaluation of an online
1025 grid-coarsening algorithm in a global eddy-admitting ocean biogeochemical model, *Journal of Advances in*
1026 *Modeling Earth Systems*, *11*(6), 1759-1783, 2019.

1027 Bouwman, A. F., Beusen, A. H. W., and Billen, G. : Human alteration of the global nitrogen and phosphorus
1028 soil balances for the period 1970–2050, *Global Biogeochemical Cycles*, *23*(4), 2009.

1029 Bouwman, A. F., Beusen, A. H. W., Overbeek, C. C., Bureau, D. P., Pawlowski, M., and Glibert, P. M.:
1030 Hindcasts and future projections of global inland and coastal nitrogen and phosphorus loads due to finfish
1031 aquaculture, *Reviews in Fisheries Science*, *21*(2), 112-156, 2013.

1032 Bouwman, A. F., Pawłowski, M., Liu, C., Beusen, A. H. W., Shumway, S. E., Glibert, P. M., and Overbeek,
1033 C. C.: Global hindcasts and future projections of coastal nitrogen and phosphorus loads due to shellfish and
1034 seaweed aquaculture, *Reviews in Fisheries Science*, *19*(4), 331-357, 2011.

1035 Buendia, E., Tanabe, K., Kranjc, A., Baasansuren, J., Fukuda, M., Ngarize, S., Osako, A., Pyrozhenko, Y.,
1036 Shermanau, P., and Federici, S.: 2019 Refinement to the 2006 IPCC Guidelines for National Greenhouse
1037 Gas Inventories*Rep.*, 2019.

1038 Buitenhuis, E. T., Suntharalingam, P., and Le Quéré, C.: Constraints on global oceanic emissions of N2O
1039 from observations and models, *Biogeosciences*, *15*(7), 2161-2175, 2018.

1040 Carroll, D., Menemenlis, D., Adkins, J. F., Bowman, K. W., Brix, H., Dutkiewicz, S., Fenty, I., Gierach,
1041 M. M., Hill, C., and Jahn, O.: The ECCO-Darwin data-assimilative global ocean biogeochemistry model:
1042 Estimates of seasonal to multidecadal surface ocean pCO2 and air-sea CO2 flux, *Journal of Advances in*
1043 *Modeling Earth Systems*, *12*(10), e2019MS001888, 2020.

1044 Chatskikh, D., Olesen, J. E., Berntsen, J., Regina, K., and Yamulki, S.: Simulation of effects of soils, climate
1045 and management on N2O emission from grasslands, *Biogeochemistry*, *76*, 395-419, 2005.

1046 Crippa, M., Solazzo, E., Guizzardi, D., Monforti-Ferrario, F., Tubiello, F. N., and Leip, A.: Food systems
1047 are responsible for a third of global anthropogenic GHG emissions, *Nature Food*, *2*(3), 198-209, 2021.

1048 Crippa, M., Solazzo, E., Guizzardi, D., Van Dingenen, R., and Leip, A.: Air pollutant emissions from global
1049 food systems are responsible for environmental impacts, crop losses and mortality, *Nature Food*, 1-15,
1050 2022.

1051 Cui, X., Zhou, F., Ciais, P., Davidson, E. A., Tubiello, F. N., Niu, X., Ju, X., Canadell, J. G., Bouwman, A.
1052 F., and Jackson, R. B.: Global mapping of crop-specific emission factors highlights hotspots of nitrous
1053 oxide mitigation, *Nature Food*, *2*(11), 886-893, 2021.

1054 Davidson, E. A., de Carvalho, C. J. R., Figueira, A. M., Ishida, F. Y., Ometto, J. P. H. B., Nardoto, G. B.,
1055 Sabá, R. T., Hayashi, S. N., Leal, E. C., and Vieira, I. C. G.: Recuperation of nitrogen cycling in Amazonian
1056 forests following agricultural abandonment, *Nature*, *447*(7147), 995-998, 2007.

1057 Davidson, E. A., Keller, M., Erickson, H. E., Verchot, L. V., and Veldkamp, E.: Testing a conceptual model
1058 of soil emissions of nitrous and nitric oxides: using two functions based on soil nitrogen availability and
1059 soil water content, the hole-in-the-pipe model characterizes a large fraction of the observed variation of
1060 nitric oxide and nitrous oxide emissions from soils, *Bioscience*, *50*(8), 667-680, 2000.

1061 Decock, C.: Mitigating nitrous oxide emissions from corn cropping systems in the midwestern US: Potential
1062 and data gaps, *Environmental Science & Technology*, *48*(8), 4247-4256, 2014.

1063 Deemer, B. R., Harrison, J. A., Li, S., Beaulieu, J. J., DelSontro, T., Barros, N., Bezerra-Neto, J. F., Powers,
1064 S. M., Dos Santos, M. A., and Vonk, J. A.: Greenhouse gas emissions from reservoir water surfaces: a new
1065 global synthesis, *BioScience*, *66*(11), 949-964, 2016.

1066 Del Grosso, S. J., Parton, W. J., Mosier, A. R., Ojima, D. S., Kulmala, A. E., and Phongpan, S.: General
1067 model for N2O and N2 gas emissions from soils due to dentrification, *Global biogeochemical cycles*, *14*(4),
1068 1045-1060, 2000.

1069 Döll, P., and Lehner, B.: Validation of a new global 30-min drainage direction map, *Journal of Hydrology*,
1070 *258*(1-4), 214-231, 2002.

26

1071 Dürr, H. H., Laruelle, G. G., van Kempen, C. M., Slomp, C. P., Meybeck, M., and Middelkoop, H.:
1072 Worldwide typology of nearshore coastal systems: defining the estuarine filter of river inputs to the oceans,
1073 *Estuaries Coasts*, *34*, 441-458, 2011.

1074 Eggleston, H. S., Buendia, L., Miwa, K., Ngara, T., and Tanabe, K. : 2006 IPCC guidelines for national
1075 greenhouse gas inventories, 2006.

1076 FAO (2020), FAO Fisheries and Aquaculture - FishStatJ - Software for Fishery and Aquaculture Statistical
1077 Time Series. In: FAO Fisheries and Aquaculture Division [online]. Rome. [Cited 3 November 2021]. ,
1078 edited.

1079 FAO (2022), FAOSTAT Climate Change, Emissions, Emissions Totals, edited.

1080 Ganesan, A. L., Manizza, M., Morgan, E. J., Harth, C. M., Kozlova, E., Lueker, T., Manning, A. J., Lunt,
1081 M. F., Mühle, J., and Lavric, J. V.: Marine nitrous oxide emissions from three Eastern Boundary Upwelling
1082 Systems inferred from atmospheric observations, *Geophysical Research Letters*, *47*(14), e2020GL087822,
1083 2020.

1084 Goldewijk, K. K., Beusen, A., Doelman, J., and Stehfest, E.: Anthropogenic land use estimates for the
1085 Holocene–HYDE 3.2, *Earth System Science Data*, *9*(2), 927-953, 2017.

1086 Hall, B. D., Dutton, G. S., and Elkins, J. W.: The NOAA nitrous oxide standard scale for atmospheric
1087 observations, *Journal of Geophysical Research: Atmospheres*, *112*(D9), 2007.

1088 Harris, I. P. D. J., Jones, P. D., Osborn, T. J., and Lister, D. H.: Updated high-resolution grids of monthly
1089 climatic observations–the CRU TS3. 10 Dataset, *International journal of climatology*, *34*(3), 623-642,
1090 2014.

1091 Heinen, M.: Simplified denitrification models: overview and properties, *Geoderma*, *133*(3-4), 444-463,
1092 2006.

1093 Helgason, B. L., Janzen, H. H., Chantigny, M. H., Drury, C. F., Ellert, B. H., Gregorich, E. G., Lemke, R.
1094 L., Pattey, E., Rochette, P., and Wagner-Riddle, C.: Toward improved coefficients for predicting direct
1095 N2O emissions from soil in Canadian agroecosystems, *Nutrient Cycling in Agroecosystems*, *72*, 87-99,
1096 2005.

1097 Hénault, C., Bizouard, F., Laville, P., Gabrielle, B., Nicoullaud, B., Germon, J. C., and Cellier, P.:
1098 Predicting in situ soil N2O emission using NOE algorithm and soil database, *Global Change Biology*, *11*(1),
1099 115-127, 2005.

1100 Hersbach, H., Bell, B., Berrisford, P., Hirahara, S., Horányi, A., Muñoz-Sabater, J., Nicolas, J., Peubey, C.,
1101 Radu, R., and Schepers, D.: Complete ERA5 from 1979: Fifth generation of ECMWF atmospheric
1102 reanalyses of the global climate, *Copernicus Climate Change Service Data Store*, 2017.

1103 Hickman, J. E., Scholes, R. J., Rosenstock, T. S., Garcia-Pando, C. P., and Nyamangara, J.: Assessing non-
1104 CO2 climate-forcing emissions and mitigation in sub-Saharan Africa, *Current Opinion in Environmental*
1105 *Sustainability*, *9*, 65-72, 2014.

1106 Hu, M., Chen, D., and Dahlgren, R. A.: Modeling nitrous oxide emission from rivers: a global assessment,
1107 *Global Change Biology*, *22*(11), 3566-3582, 2016.

1108 Huang, Y., and Gerber, S.: Global soil nitrous oxide emissions in a dynamic carbon-nitrogen model,
1109 *Biogeosciences*, *12*(21), 6405-6427, 2015.

1110 Hurtt, G. C., Chini, L., Sahajpal, R., Frolking, S., Bodirsky, B. L., Calvin, K., Doelman, J. C., Fisk, J.,
1111 Fujimori, S., and Klein Goldewijk, K.: Harmonization of global land use change and management for the
1112 period 850–2100 (LUH2) for CMIP6, *Geoscientific Model Development*, *13*(11), 5425-5464, 2020.

1113 IEA: World Energy Outlook 2021*Rep.*, IEA, Paris, 2021.

1114   Inatomi, M., Ito, A., Ishijima, K., and Murayama, S.: Greenhouse gas budget of a cool-temperate deciduous
1115   broad-leaved forest in Japan estimated using a process-based model, *Ecosystems*, *13*, 472-483, 2010.

1116   IPCC: Revised 1996 IPCC Guidelines for National Greenhouse Gas Inventories, 1996.

1117   IPCC: Good practice guidance and uncertainty management in national greenhouse gas inventories, 2000.

1118   IPCC: IPCC Guidelines for National Greenhouse Gas Inventories*Rep.*, Hayama, Japan, 2006.

1119   Ito, A., Nishina, K., Ishijima, K., Hashimoto, S., and Inatomi, M.: Emissions of nitrous oxide (N 2 O) from
1120   soil surfaces and their historical changes in East Asia: a model-based assessment, *Progress in Earth*
1121   *Planetary Science*, *5*, 1-13, 2018.

1122   Janssens-Maenhout, G., Crippa, M., Guizzardi, D., Muntean, M., Schaaf, E., Dentener, F., Bergamaschi,
1123   P., Pagliari, V., Olivier, J. G., and Peters, J. A.: EDGAR v4. 3.2 Global Atlas of the three major greenhouse
1124   gas emissions for the period 1970–2012, *Earth System Science Data*, *11*(3), 959-1002, 2019.

1125   Jin, X., and Gruber, N.: Offsetting the radiative benefit of ocean iron fertilization by enhancing N2O
1126   emissions, *Geophysical research letters*, *30*(24), 2003.

1127   Johnson, D. J., Niedbalski, N. P., Ervin, J. S., and Patnaik, S. S.: Ammonium carbamate-based heat
1128   exchanger reactor as an endothermic heat sink for thermal management, *International Journal of Heat Mass*
1129   *Transfer*, *91*, 766-776, 2015.

1130   Kalnay, E., Kanamitsu, M., Kistler, R., Collins, W., Deaven, D., Gandin, L., Iredell, M., Saha, S., White,
1131   G., and Woollen, J.: The NCEP/NCAR 40-year reanalysis project, *Bulletin of the American meteorological*
1132   *Society*, *77*(3), 437-472, 1996.

1133   Keller, M., and Reiners, W. A.: Soil-atmosphere exchange of nitrous oxide, nitric oxide, and methane under
1134   secondary succession of pasture to forest in the Atlantic lowlands of Costa Rica, *Global Biogeochemical*
1135   *Cycles*, *8*(4), 399-409, 1994.

1136   Kim, D.-G., Giltrap, D., and Hernandez-Ramirez, G.: Background nitrous oxide emissions in agricultural
1137   and natural lands: a meta-analysis, *Plant Soil*, *373*, 17-30, 2013a.

1138   Kim, D.-G., Hernandez-Ramirez, G., and Giltrap, D.: Linear and nonlinear dependency of direct nitrous
1139   oxide emissions on fertilizer nitrogen input: A meta-analysis, *Agriculture, Ecosystems Environment*, *168*,
1140   53-65, 2013b.

1141   Kock, A., and Bange, H. W.: Counting the ocean's greenhouse gas emissions, *Eos: Earth Space Science*
1142   *News*, *96*(3), 10-13, 2015.

1143   Kou Giesbrecht, S., and Arora, V. K.: Representing the dynamic response of vegetation to nitrogen
1144   limitation via biological nitrogen fixation in the CLASSIC Land Model, *Global Biogeochemical Cycles*,
1145   *36*(6), e2022GB007341, 2022.

1146   Landolfi, A., Somes, C. J., Koeve, W., Zamora, L. M., and Oschlies, A.: Oceanic nitrogen cycling and N2O
1147   flux perturbations in the Anthropocene, *Global Biogeochemical Cycles*, *31*(8), 1236-1255, 2017.

1148   Laruelle, G. G., Landschützer, P., Gruber, N., Tison, J.-L., Delille, B., and Regnier, P.: Global high-
1149   resolution monthly pCO2 climatology for the coastal ocean derived from neural network interpolation,
1150   *Biogeosciences*, *14*(19), 4545-4561, 2017.

1151   Lauerwald, R., Regnier, P., Figueiredo, V., Enrich-Prast, A., Bastviken, D., Lehner, B., Maavara, T., and
1152   Raymond, P.: Natural lakes are a minor global source of N2O to the atmosphere, *Global Biogeochemical*
1153   *Cycles*, *33*(12), 1564-1581, 2019.

1154   Le Quéré, C., Buitenhuis, E. T., Moriarty, R., Alvain, S., Aumont, O., Bopp, L., Chollet, S., Enright, C.,
1155   Franklin, D. J., and Geider, R. J.: Role of zooplankton dynamics for Southern Ocean phytoplankton biomass
1156   and global biogeochemical cycles, *Biogeosciences*, *13*(14), 4111-4133, 2016.

1157 Lehner, B., Liermann, C. R., Revenga, C., Vörösmarty, C., Fekete, B., Crouzet, P., Döll, P., Endejan, M.,
1158 Frenken, K., and Magome, J. : High-resolution mapping of the world's reservoirs and dams for sustainable
1159 river-flow management, *Frontiers in Ecology the Environment*, *9*(9), 494-502, 2011.

1160 Lehner, B., Verdin, K., and Jarvis, A.: New global hydrography derived from spaceborne elevation data,
1161 *Eos, Transactions American Geophysical Union*, *89*(10), 93-94, 2008.

1162 Lehuger, S., Gabrielle, B., Laville, P., Lamboni, M., Loubet, B., and Cellier, P.: Predicting and mitigating
1163 the net greenhouse gas emissions of crop rotations in Western Europe, *Agricultural Forest Meteorology*,
1164 *151*(12), 1654-1671, 2011.

1165 Leppelt, T., Dechow, R., Gebbert, S., Freibauer, A., Lohila, A., Augustin, J., Drösler, M., Fiedler, S.,
1166 Glatzel, S., and Höper, H.: Nitrous oxide emission budgets and land-use-driven hotspots for organic soils
1167 in Europe, *Biogeosciences*, *11*(23), 6595-6612, 2014.

1168 Lan, X., E.J. Dlugokencky, J.W. Mund, A.M. Crotwell, M.J. Crotwell, E. Moglia, M. Madronich, D. Neff
1169 and   K.W.   Thoning   (2022),   Atmospheric   Nitrous   Oxide   Dry   Air
1170 Mole Fractions from the NOAA GML Carbon Cycle Cooperative Global Air Sampling Network,
1171 1997-2021, Version: 2022-11-21, https://doi.org/10.15138/53g1-x417

1172 Li, C., Aber, J., Stange, F., Butterbach-Bahl, K., and Papen, H.: A process-oriented model of N2O and NO
1173 emissions from forest soils: 1. Model development, *Journal of Geophysical Research: Atmospheres*,
1174 *105*(D4), 4369-4384, 2000.

1175 Li, C., Frolking, S., and Frolking, T. A.: A model of nitrous oxide evolution from soil driven by rainfall
1176 events: 2. Model applications, *Journal of Geophysical Research: Atmospheres*, *97*(D9), 9777-9783, 1992.

1177 Liang, J. H., Deutsch, C., McWilliams, J. C., Baschek, B., Sullivan, P. P., and Chiba, D.: Parameterizing
1178 bubble-mediated air-sea gas exchange and its effect on ocean ventilation, *Global Biogeochemical Cycles*,
1179 *27*(3), 894-905, 2013.

1180 Lu, C., and Tian, H.: Net greenhouse gas balance in response to nitrogen enrichment: perspectives from a
1181 coupled biogeochemical model, *Global Change Biology*, *19*(2), 571-588, 2013.

1182 Maavara, T., Lauerwald, R., Laruelle, G. G., Akbarzadeh, Z., Bouskill, N. J., Van Cappellen, P., and
1183 Regnier, P.: Nitrous oxide emissions from inland waters: Are IPCC estimates too high?, *Global Change*
1184 *Biology*, *25*(2), 473-488, 2019.

1185 Madec, G.: NEMO ocean engine: Note du pole de modélisation, Institut Pierre-Simon Laplace (IPSL),
1186 France, No 27 ISSN No 1288-1619, *France: IPSL*, 2008.

1187 Madec, G., Bourdallé-Badie, R., Bouttier, P.-A., Bricaud, C., Bruciaferri, D., Calvert, D., Chanut, J.,
1188 Clementi, E., Coward, A., and Delrosso, D.: NEMO ocean engine, 2017.

1189 Manizza, M., Keeling, R. F., and Nevison, C. D.: On the processes controlling the seasonal cycles of the
1190 air–sea fluxes of O2 and N2O: A modelling study, *Tellus B: Chemical Physical Meteorology*, *64*(1), 18429,
1191 2012.

1192 Manizza, M., Menemenlis, D., Zhang, H., and Miller, C. E.: Modeling the recent changes in the Arctic
1193 Ocean CO2 sink (2006–2013), *Global Biogeochemical Cycles*, *33*(3), 420-438, 2019.

1194 Martinez-Rey, J., Bopp, L., Gehlen, M., Tagliabue, A., and Gruber, N.: Projections of oceanic N2O
1195 emissions in the 21st century using the IPSL Earth system model, *Biogeosciences*, *12*(13), 4133-4148, 2015.

1196 Marzadri, A., Amatulli, G., Tonina, D., Bellin, A., Shen, L. Q., Allen, G. H., and Raymond, P. A.: Global
1197 riverine nitrous oxide emissions: The role of small streams and large rivers, *Science of The Total*
1198 *Environment*, *776*, 145148, 2021.

1199 Marzadri, A., Dee, M. M., Tonina, D., Bellin, A., and Tank, J. L.: Role of surface and subsurface processes
1200 in scaling N2O emissions along riverine networks, *Proceedings of the National Academy of Sciences*,
1201 *114*(17), 4330-4335, 2017.

1202 McCrackin, M. L., Harrison, J. A., and Compton, J. E.: Factors influencing export of dissolved inorganic
1203 nitrogen by major rivers: A new, seasonal, spatially explicit, global model, *Global Biogeochemical Cycles*,
1204 *28*(3), 269-285, 2014.

1205 Melillo, J. M., Steudler, P. A., Feigl, B. J., Neill, C., Garcia, D., Piccolo, M. C., Cerri, C. C., and Tian, H.:
1206 Nitrous oxide emissions from forests and pastures of various ages in the Brazilian Amazon, *Journal of
1207 Geophysical Research: Atmospheres*, *106*(D24), 34179-34188, 2001.

1208 Messager, M. L., Lehner, B., Grill, G., Nedeva, I., and Schmitt, O.: Estimating the volume and age of water
1209 stored in global lakes using a geo-statistical approach, *Nature Communications*, *7*(1), 13603, 2016.

1210 Nevison, C., Butler, J. H., and Elkins, J. W.: Global distribution of N2O and the ΔN2O-AOU yield in the
1211 subsurface ocean, *Global Biogeochemical Cycles*, *17*(4), 2003.

1212 Pan, S., Bian, Z., Tian, H., Yao, Y., Najjar, R. G., Friedrichs, M. A. M., Hofmann, E. E., Xu, R., and Zhang,
1213 B.: Impacts of multiple environmental changes on long-term nitrogen loading from the Chesapeake Bay
1214 watershed, *Journal of Geophysical Research: Biogeosciences*, *126*(5), e2020JG005826, 2021.

1215 Parekh, P., Joos, F., and Müller, S. A.: A modeling assessment of the interplay between aeolian iron fluxes
1216 and iron-binding ligands in controlling carbon dioxide fluctuations during Antarctic warm events,
1217 *Paleoceanography*, *23*(4), 2008.

1218 Parton, W. J., Mosier, A. R., Ojima, D. S., Valentine, D. W., Schimel, D. S., Weier, K., and Kulmala, A.
1219 E.: Generalized model for N2 and N2O production from nitrification and denitrification, *Global
1220 biogeochemical cycles*, *10*(3), 401-412, 1996.

1221 Patra, P. K., Dlugokencky, E. J., Elkins, J. W., Dutton, G. S., Tohjima, Y., Sasakawa, M., Ito, A., Weiss,
1222 R. F., Manizza, M., and Krummel, P. B.: Forward and inverse modelling of atmospheric nitrous oxide using
1223 MIROC4-atmospheric chemistry-transport model, *Journal of the Meteorological Society of Japan. Ser. II*,
1224 *100*(2), 361-386, 2022.

1225 Patra, P. K., Takigawa, M., Watanabe, S., Chandra, N., Ishijima, K., and Yamashita, Y.: Improved chemical
1226 tracer simulation by MIROC4. 0-based atmospheric chemistry-transport model (MIROC4-ACTM), *Sola*,
1227 *14*, 91-96, 2018.

1228 Paulot, F., Jacob, D. J., Johnson, M. T., Bell, T. G., Baker, A. R., Keene, W. C., Lima, I. D., Doney, S. C.,
1229 and Stock, C. A.: Global oceanic emission of ammonia: Constraints from seawater and atmospheric
1230 observations, *Global Biogeochemical Cycles*, *29*(8), 1165-1178, 2015.

1231 Peltier, W. R.: Global glacial isostasy and the surface of the ice-age Earth: the ICE-5G (VM2) model and
1232 GRACE, *Annual Review of Earth and Planetary Sciences*, *32*, 111-149, 2004.

1233 Portmann, F. T., Siebert, S., and Döll, P.: MIRCA2000—Global monthly irrigated and rainfed crop areas
1234 around the year 2000: A new high-resolution data set for agricultural and hydrological modeling, *Global
1235 Biogeochemical Cycles*, *24*(1), 2010.

1236 Porwollik, V., Rolinski, S., Heinke, J., and Müller, C.: Generating a rule-based global gridded tillage
1237 dataset, *Earth System Science Data*, *11*(2), 823-843, 2019.

1238 Prather, M. J., Hsu, J., DeLuca, N. M., Jackman, C. H., Oman, L. D., Douglass, A. R., Fleming, E. L.,
1239 Strahan, S. E., Steenrod, S. D., and Søvde, O. A.: Measuring and modeling the lifetime of nitrous oxide
1240 including its variability, *Journal of Geophysical Research: Atmospheres*, *120*(11), 5693-5705, 2015.

1241 Rochette, P., and Janzen, H. H.: Towards a revised coefficient for estimating N2O emissions from legumes,
1242 *Nutrient Cycling in Agroecosystems*, *73*, 171-179, 2005.

Rosentreter, J. A., Laruelle, G. G., Bange, H. W., Bianchi, T. S., Busecke, J. J. M., Cai, W.-J., Eyre, B. D., Forbrich, I., Kwon, E. Y., and Maavara, T.: Coastal vegetation and estuaries are collectively a greenhouse gas sink, *Nature Climate Change*, 1-9, 2023.

Sacks, W. J., Deryng, D., Foley, J. A., and Ramankutty, N.: Crop planting dates: an analysis of global patterns, *Global Ecology Biogeography*, *19*(5), 607-620, 2010.

Salas y Mélia, D.: A global coupled sea ice–ocean model, *Ocean Modelling*, *4*(2), 137-172, 2002.

Séférian, R., Nabat, P., Michou, M., Saint-Martin, D., Voldoire, A., Colin, J., Decharme, B., Delire, C., Berthet, S., and Chevallier, M.: Evaluation of CNRM Earth System Model, CNRM-ESM2-1: role of Earth system processes in present-day and future climate, *Journal of Advances in Modeling Earth Systems*, *11*(12), 4182-4227, 2019.

Shangguan, W., Dai, Y., Duan, Q., Liu, B., and Yuan, H.: A global soil data set for earth system modeling, *Journal of Advances in Modeling Earth Systems*, *6*(1), 249-263, 2014.

Shcherbak, I., Millar, N., and Robertson, G. P.: Global metaanalysis of the nonlinear response of soil nitrous oxide (N2O) emissions to fertilizer nitrogen, *Proceedings of the National Academy of Sciences*, *111*(25), 9199-9204, 2014.

Shu, S., Jain, A. K., Koven, C. D., and Mishra, U.: Estimation of permafrost SOC stock and turnover time using a land surface model with vertical heterogeneity of permafrost soils, *Global Biogeochemical Cycles*, *34*(11), e2020GB006585, 2020.

Solazzo, E., Crippa, M., Guizzardi, D., Muntean, M., Choulga, M., and Janssens-Maenhout, G.: Uncertainties in the Emissions Database for Global Atmospheric Research (EDGAR) emission inventory of greenhouse gases, *Atmospheric Chemistry Physics*, *21*(7), 5655-5683, 2021.

Stehfest, E., and Bouwman, L.: N2O and NO emission from agricultural fields and soils under natural vegetation: summarizing available measurement data and modeling of global annual emissions, *Nutrient cycling in agroecosystems*, *74*, 207-228, 2006.

Sullivan, B. W., Nifong, R. L., Nasto, M. K., Alvarez-Clare, S., Dencker, C. M., Soper, F. M., Shoemaker, K. T., Ishida, F. Y., Zaragoza-Castells, J., and Davidson, E. A.: Biogeochemical recuperation of lowland tropical forest during succession, *Ecology*, *100*(4), e02641, 2019.

Tarantola, A.: *Inverse problem theory and methods for model parameter estimation*, SIAM, 2005.

Thompson, R. L., Chevallier, F., Crotwell, A. M., Dutton, G., Langenfelds, R. L., Prinn, R. G., Weiss, R. F., Tohjima, Y., Nakazawa, T., and Krummel, P. B.: Nitrous oxide emissions 1999 to 2009 from a global atmospheric inversion, *Atmospheric Chemistry Physics*, *14*(4), 1801-1817, 2014.

Thornton, P. E., and Rosenbloom, N. A. : Ecosystem model spin-up: Estimating steady state conditions in a coupled terrestrial carbon and nitrogen cycle model, *Ecological Modelling*, *189*(1-2), 25-48, 2005.

Tian, H., Bian, Z., Shi, H., Qin, X., Pan, N., Lu, C., Pan, S., Tubiello, F. N., Chang, J., and Conchedda, G.: History of anthropogenic Nitrogen inputs (HaNi) to the terrestrial biosphere: a 5 arcmin resolution annual dataset from 1860 to 2019, *Earth System Science Data*, *14*(10), 4551-4568, 2022.

Tian, H., Chen, G., Zhang, C., Liu, M., Sun, G., Chappelka, A., Ren, W., Xu, X., Lu, C., and Pan, S.: Century-scale responses of ecosystem carbon storage and flux to multiple environmental changes in the southern United States, *Ecosystems*, *15*, 674-694, 2012a.

Tian, H., Lu, C., Chen, G., Tao, B., Pan, S., Grosso, S. J. D., Xu, X., Bruhwiler, L., Wofsy, S. C., and Kort, E. A.: Contemporary and projected biogenic fluxes of methane and nitrous oxide in North American terrestrial ecosystems, *Frontiers in Ecology the Environment*, *10*(10), 528-536, 2012b.

1285 Tian, H., Ren, W., Yang, J., Tao, B., Cai, W. J., Lohrenz, S. E., Hopkinson, C. S., Liu, M., Yang, Q., and
1286 Lu, C. : Climate extremes dominating seasonal and interannual variations in carbon export from the
1287 Mississippi River Basin, *Global Biogeochemical Cycles*, *29*(9), 1333-1347, 2015.

1288 Tian, H., Xu, R., Canadell, J. G., Thompson, R. L., Winiwarter, W., Suntharalingam, P., Davidson, E. A.,
1289 Ciais, P., Jackson, R. B., Janssens-Maenhout, G., ..., and Yuanzhi, Y.: A comprehensive quantification of
1290 global nitrous oxide sources and sinks, *Nature*, *586*(7828), 248-256, 2020a.

1291 Tian, H., Xu, R., Pan, S., Yao, Y., Bian, Z., Cai, W. J., Hopkinson, C. S., Justic, D., Lohrenz, S., and Lu,
1292 C.: Long-term trajectory of nitrogen loading and delivery from Mississippi River Basin to the Gulf of
1293 Mexico, *Global Biogeochemical Cycles*, *34*(5), e2019GB006475, 2020b.

1294 Tian, H., Xu, X., Liu, M., Ren, W., Zhang, C., Chen, G., and Lu, C.: Spatial and temporal patterns of CH_4
1295 and N_2O fluxes in terrestrial ecosystems of North America during 1979–2008: application of a global
1296 biogeochemistry model, *Biogeosciences*, *7*(9), 2673-2694, 2010.

1297 Tian, H., Xu, X., Lu, C., Liu, M., Ren, W., Chen, G., Melillo, J., and Liu, J.: Net exchanges of CO_2, CH_4,
1298 and N_2O between China's terrestrial ecosystems and the atmosphere and their contributions to global
1299 climate warming, *Journal of Geophysical Research: Biogeosciences*, *116*(G2), 2011.

1300 Tian, H., Yang, J., Lu, C., Xu, R., Canadell, J. G., Jackson, R. B., Arneth, A., Chang, J., Chen, G., and
1301 Ciais, P.: The global N2O model intercomparison project, *Bulletin of the American Meteorological Society*,
1302 *99*(6), 1231-1251, 2018.

1303 Tian, H., R. Xu, S. Pan, Y. Yao, Z. Bian, W. J. Cai, C. S. Hopkinson, D. Justic, S. Lohrenz, C. Lu, W. Ren,
1304 and J. Yang. (2020). Long-Term Trajectory of Nitrogen Loading and Delivery From Mississippi River
1305 Basin to the Gulf of Mexico. *Global Biogeochemical Cycles*, *34*(5), e2019GB006475.
1306 https://doi.org/10.1029/2019GB006475.

1307 Tschumi, T., Joos, F., Gehlen, M., and Heinze, C.: Deep ocean ventilation, carbon isotopes, marine
1308 sedimentation and the deglacial CO_2 rise, *Climate of the Past*, *7*(3), 771-800, 2011.

1309 Tsujino, H., Urakawa, L. S., Griffies, S. M., Danabasoglu, G., Adcroft, A. J., Amaral, A. E., Arsouze, T.,
1310 Bentsen, M., Bernardello, R., and Böning, C. W.: Evaluation of global ocean–sea-ice model simulations
1311 based on the experimental protocols of the Ocean Model Intercomparison Project phase 2 (OMIP-2),
1312 *Geoscientific Model Development*, *13*(8), 3643-3708, 2020.

1313 Tsujino, H., Urakawa, S., Nakano, H., Small, R. J., Kim, W. M., Yeager, S. G., Danabasoglu, G., Suzuki,
1314 T., Bamber, J. L., and Bentsen, M.: JRA-55 based surface dataset for driving ocean–sea-ice models (JRA55-
1315 do), *Ocean Modelling*, *130*, 79-139, 2018.

1316 Van Drecht, G., Bouwman, A. F., Harrison, J., and Knoop, J. M.: Global nitrogen and phosphate in urban
1317 wastewater for the period 1970 to 2050, *Global Biogeochemical Cycles*, *23*(4), 2009.

1318 Van Drecht, G., Bouwman, A. F., Knoop, J. M., Beusen, A. H. W., and Meinardi, C. R.: Global modeling
1319 of the fate of nitrogen from point and nonpoint sources in soils, groundwater, and surface water, *Global
1320 Biogeochemical Cycles*, *17*(4), 2003.

1321 Verchot, L. V., Davidson, E. A., Cattânio, H., Ackerman, I. L., Erickson, H. E., and Keller, M.: Land use
1322 change and biogeochemical controls of nitrogen oxide emissions from soils in eastern Amazonia, *Global
1323 Biogeochemical Cycles*, *13*(1), 31-46, 1999.

1324 Walter, K., Don, A., Fuß, R., Kern, J., Drewer, J., and Flessa, H.: Direct nitrous oxide emissions from
1325 oilseed rape cropping–a meta-analysis, *Gcb Bioenergy*, *7*(6), 1260-1271, 2015.

1326 Wang, Q., Zhou, F., Shang, Z., Ciais, P., Winiwarter, W., Jackson, R. B., Tubiello, F. N., Janssens-
1327 Maenhout, G., Tian, H., and Cui, X.: Data-driven estimates of global nitrous oxide emissions from
1328 croplands, *National Science Review*, *7*(2), 441–452, 2020.

Wanninkhof, R.: Relationship between wind speed and gas exchange over the ocean, *Journal of Geophysical Research: Oceans*, *97*(C5), 7373-7382, 1992.

Wanninkhof, R.: Relationship between wind speed and gas exchange over the ocean revisited, *Limnology Oceanography: Methods*, *12*(6), 351-362, 2014.

Weiss, R. F., and Price, B. A.: Nitrous oxide solubility in water and seawater, *Marine Chemistry*, *8*(4), 347-359, 1980.

Wells, K. C., Millet, D. B., Bousserez, N., Henze, D. K., Chaliyakunnel, S., Griffis, T. J., Luan, Y., Dlugokencky, E. J., Prinn, R. G., and O'Doherty, S.: Simulation of atmospheric N 2 O with GEOS-Chem and its adjoint: evaluation of observational constraints, *Geoscientific Model Development*, *8*(10), 3179-3198, 2015.

Wilson, C., Chipperfield, M. P., Gloor, M., and Chevallier, F.: Development of a variational flux inversion system (INVICAT v1. 0) using the TOMCAT chemical transport model, *Geoscientific Model Development*, *7*(5), 2485-2500, 2014.

Wollheim, W. M., Vörösmarty, C. J., Bouwman, A. F., Green, P., Harrison, J., Linder, E., Peterson, B. J., Seitzinger, S. P., and Syvitski, J. P. M.: Global N removal by freshwater aquatic systems using a spatially distributed, within-basin approach, *Global Biogeochemical Cycles*, *22*(2), 2008.

Xu-Ri, and Prentice, I. C.: Terrestrial nitrogen cycle simulation with a dynamic global vegetation model, *Global Change Biology*, *14*(8), 1745-1764, 2008.

Xu, R., Tian, H., Lu, C., Pan, S., Chen, J., Yang, J., and Zhang, B.: Preindustrial nitrous oxide emissions from the land biosphere estimated by using a global biogeochemistry model, *Climate of the Past*, *13*(7), 977-990, 2017.

Xu, X., Sharma, P., Shu, S., Lin, T.-S., Ciais, P., Tubiello, F. N., Smith, P., Campbell, N., and Jain, A. K.: Global greenhouse gas emissions from animal-based foods are twice those of plant-based foods, *Nature Food*, *2*(9), 724-732, 2021.

Xu, X., Tian, H., Liu, M., Ren, W., Chen, G., Lu, C., and Zhang, C.: Multiple-factor controls on terrestrial N2O flux over North America from 1979 through 2010, *Biogeosciences Discussions*, *8*(6), 2011.

Yang, H., Zhou, F., Piao, S., Huang, M., Chen, A., Ciais, P., Li, Y., Lian, X., Peng, S., and Zeng, Z.: Regional patterns of future runoff changes from Earth system models constrained by observation, *Geophysical Research Letters*, *44*(11), 5540-5549, 2017.

Yang, Q., Tian, H., Friedrichs, M. A. M., Hopkinson, C. S., Lu, C., and Najjar, R. G.: Increased nitrogen export from eastern North America to the Atlantic Ocean due to climatic and anthropogenic changes during 1901–2008, *Journal of Geophysical Research: Biogeosciences*, *120*(6), 1046-1068, 2015.

Yang, S., Chang, B. X., Warner, M. J., Weber, T. S., Bourbonnais, A. M., Santoro, A. E., Kock, A., Sonnerup, R. E., Bullister, J. L., and Wilson, S. T.: Global reconstruction reduces the uncertainty of oceanic nitrous oxide emissions and reveals a vigorous seasonal cycle, *Proceedings of the National Academy of Sciences*, *117*(22), 11954-11960, 2020.

Yang, X., Wittig, V., Jain, A. K., and Post, W.: Integration of nitrogen cycle dynamics into the Integrated Science Assessment Model for the study of terrestrial ecosystem responses to global change, *Global Biogeochemical Cycles*, *23*(4), 2009.

Yao, Y., Tian, H., Shi, H., Pan, S., Xu, R., Pan, N., and Canadell, J. G.: Increased global nitrous oxide emissions from streams and rivers in the Anthropocene, *Nature Climate Change*, *10*(2), 138-142, 2020.

Yao, Y., Tian, H., Xu, X., Li, Y., and Pan, S.: Dynamics and controls of inland water CH4 emissions across the Conterminous United States: 1860-2019, *Water Research*, *224*, 119043, 2022.

1372 Yool, A., Martin, A. P., Fernández, C., and Clark, D. R.: The significance of nitrification for oceanic new
1373 production, *Nature*, *447*(7147), 999-1002, 2007.

1374 Zaehle, S., Ciais, P., Friend, A. D., and Prieur, V.: Carbon benefits of anthropogenic reactive nitrogen
1375 offset by nitrous oxide emissions, *Nature Geoscience*, *4*(9), 601-605, 2011.

1376 Zaehle, S., and Friend, A. D.: Carbon and nitrogen cycle dynamics in the O-CN land surface model: 1.
1377 Model description, site-scale evaluation, and sensitivity to parameter estimates, *Global Biogeochemical*
1378 *Cycles*, *24*(1), 2010.

1379 Zamora, L. M., and Oschlies, A.: Surface nitrification: A major uncertainty in marine N2O emissions,
1380 *Geophysical Research Letters*, *41*(12), 4247-4253, 2014.

1381 Zhang, Y., Li, C., Zhou, X., and Moore III, B.: A simulation model linking crop growth and soil
1382 biogeochemistry for sustainable agriculture, *Ecological Modelling*, *151*(1), 75-108, 2002.

1383 Zhou, F., Shang, Z., Zeng, Z., Piao, S., Ciais, P., Raymond, P. A., Wang, X., Wang, R., Chen, M., and
1384 Yang, C.: New model for capturing the variations of fertilizer-induced emission factors of N2O, *Global*
1385 *Biogeochemical Cycles*, *29*(6), 885-897, 2015.

1386 Zhou, J. B., Jiang, M. M., and Chen, G. Q.: Estimation of methane and nitrous oxide emission from
1387 livestock and poultry in China during 1949–2003, *Energy Policy*, *35*(7), 3759-3767, 2007.

1388 Zhu, Q., Riley, W. J., Tang, J., and Koven, C. D. : Multiple soil nutrient competition between plants,
1389 microbes, and mineral surfaces: model development, parameterization, and example applications in
1390 several tropical forests, *Biogeosciences*, *13*(1), 341-363, 2016.